ELSEVIER

Journal of Magnetism and Magnetic Materials 200 (1999) 1–23

Journal of magnetism and magnetic materials

www.elsevier.com/locate/jmmm

Colossal magnetoresistive manganites

Y. Tokura[a,*], Y. Tomioka[b]

[a]Department of Applied Physics, University of Tokyo, Tokyo 113-8656, Japan
[b]Joint Research Center for Atom technology, Tsukuba 305-0046, Japan

Received 20 January 1999; received in revised form 10 March 1999; accepted 10 March 1999

Abstract

Magnetoelectronic features of the perovskite-type manganites are overviewed in the light of the mechanism of the colossal magnetoresistance (CMR). The essential ingredient of the CMR physics is not only the double-exchange interaction but also other competing interactions, such as ferromagnetic/antiferromagnetic superexchange interactions and charge/orbital ordering instabilities as well as their strong coupling with the lattice deformation. In particular, the orbital degree of freedom of the conduction electrons in the near-degenerate 3d e_g state plays an essential role in producing the unconventional metal–insulator phenomena in the manganites via strong coupling with spin, charge, and lattice degrees of freedom. Insulating or poorly conducting states arise from the long or short-range correlations of charge and orbital, but can be mostly melted or turned into the orbital-disordered conducting state by application of a magnetic field, producing the CMR or the insulator–metal transition.

Keywords: Colossal magnetoresistance; Manganese oxides; Double-exchange interaction; Orbital ordering; Charge ordering

1. Introduction

The particular magnetoresistance (MR) phenomena described here are the gigantic decrease of resistance by application of a magnetic field that is observed for the manganese oxides (manganites) with perovskite or related structures [1]. Such a gigantic negative MR is now termed "colossal magnetoresistance" (CMR) to distinguish it from the giant magnetoresistance (GMR) observed in transtion metal systems in multilayer or granular forms. The MR in the perovskite manganites near the Curie temperature (T_C) seems to have already been known at the very early stage of the study on transition metal oxides. For example, the paper in 1969 by Searle and Wang [2] reported thoroughly the magnetic field dependence of the resistivity for a flux-grown crystal of $La_{1-x}Pb_xMnO_3$; in particular the large MR near T_C, as well as the phenomenological analysis. Soon after, Kubo and Ohata [3] have given a theoretical account for this phenomenon using the so-called double-exchange Hamiltonian (or the s–d model with the on-site ferromagnetic exchange interaction), that includes the essential ingredient of the double-exchange mechanism elaborated by Zener [4], Anderson and Hasegawa [5], and de Gennes [6]. Interest in the MR of those manganites has revived more lately since the rediscovery of the CMR or even more

* Corresponding author. Tel.: +81-3-5841-6870; fax: +81-3-3816-3992.
E-mail address: tokura@ap.t.u-tokyo.ac.jp (Y. Tokura)

0304-8853/99/$ - see front matter
PII: S0304-8853(99)00352-2

astonishing magnetic field induced insulator–metal [7–11] and/or lattice-structural [12] transitions. On the one hand, the highly sensitive and electrically readable magnetic-field sensors have recently been in industrial demand for the read-head of the magnetic memory and it is anticipated that the CMR oxides may be one such candidate material.

The "renaissance" of the CMR manganites was due partly to the revived interest in the barely metallic state of the transition metal oxides with strong electron–electron and/or electron–lattice interaction since the discovery of the high-temperature superconductivity in copper oxide (cuprate) compounds. After the experience of the research fever for superconducting cuprates, there has been much progress in the preparative method of oxide specimens, e.g., growth of single crystals and fabrication of epitaxial thin films, as well as in comprehensive understanding of the electronic and magnetic properties of such correlated-electron systems [13]. This circumstance has expedited the research on the CMR oxides, as of nowadays.

In perovskite-related structures (Fig. 1), the two important parameters, i.e., the band filling (or doping level) and the bandwidth (or electron hopping interaction), can be controlled to a considerable extent by modifying the chemical composition of the perovskite. Both the parameters control the kinetic energy of the conduction electrons which not only governs the metal–insulator phenomena but also the competing magnetic interactions, i.e. ferromagnetic vs. antiferromagnetic, in the perovskite manganites. We will see ample examples of the chemical control of the electronically important parameters in the following.

In this article, we first overview fundamental electronic and lattice features (Section 2) for perovskite manganites. After describing the electronic configuration and double-exchange interaction of Mn ions placed in the perovskite lattice, we focus on the experimentally observed features of magnetoresistance and insulator–metal transition for $La_{1-x}Sr_xMnO_3$ crystals that are viewed as the most typical double-exchange systems although many important deviations from the simple model already show up there. Section 3 is devoted to the description on the compositional tuning of the CMR effect in perovskite manganites. We present

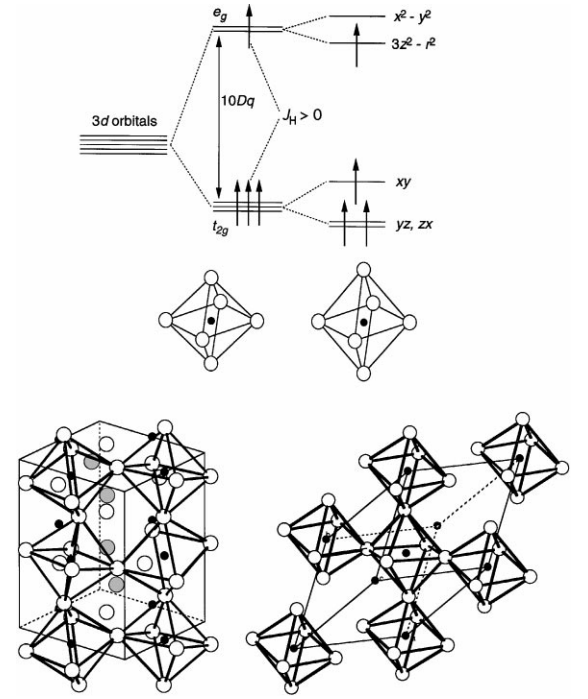

Fig. 1. Upper panel: crystal-field splitting of five-fold degenerate atomic 3d levels into lower t_{2g}(triply degenerate) and higher e_g (doubly degenerate) levels. Jahn–Teller distortion of MnO_6 octahedron further lifts each degeneracy. Lower panel: Schematic structures of distorted perovskites of manganite; orthorhombic (left) and rhombohedral (right).

electronic phase daigrams in the plane of temperature and hole-doping level for representative manganites and specify the compositional region where the CMR is most pronounced. As a most remakable example of the CMR, we describe in Section 4 the magnetic field-induced melting of the charge/orbital ordered states which are widely observed in heavily hole-doped manganites (around $x = 0.5$). We present the systematic electronic phase diagrams relevant to the charge/orbital ordering with variation of the electronic bandwidth at $x = 1/2$ as well as of the hole doping level away from $x = 1/2$, which are the bases of the magnetic or photonic metal-insulator phase control of these manganites. In Section 5 we briefly review late advances in study on the layered-structure manganites which show many unconventional

magnetoelectronic and magnetoelastic properties, including the CMR effect.

2. Fundamental electronic and lattice features

2.1. Electronic features

The manganese (Mn) ion in the CMR manganite is surrounded by the oxygen octahedron. The 3d orbitals on the Mn-site placed in such an octahedral coordination are subject to the partial lifting of the degeneracy into lower-lying t_{2g} states and higher-lying e_g sates. In the Mn^{3+}-based compounds, the Mn site shows the electronic configuration of $t_{2g}^3 e_g^1$ (total spin number $S = 2$). The t_{2g} electrons, less hybridized with 2_p states and stabilized by the crystal field splitting, are viewed as always localized by the strong correlation effect and as forming the local spin ($S = 3/2$) even in the metallic state. Even the e_g state electrons, hybridized strongly with O 2p states, are affected by such a correlation effect, and tend to localize in the "carrier-undoped" or the parent all-Mn^{3+}-based compound, forming the so-called Mott insulator. However, the e_g electrons can be itinerant and hence play a role of conduction electrons, when electron vacancies or holes are created in the e_g orbital states of the crystal. The latter hole-doping procedure corresponds to creation of mobile Mn^{4+} species on the Mn sites.

The important consequence of the apparent separation into the spin and charge sectors in the 3d orbital states is the effective strong coupling between the e_g conduction electron spin ($S = 1/2$) and t_{2g} electron local spin ($S = 3/2$). This on-site ferromagnetic coupling follows the Hund's rule. The exchange energy J_H (Hund's-rule coupling energy) is as large as 2–3 eV for the manganites and exceeds the intersite hopping interaction t_{ij}^0 of the e_g electron between the neighboring sites, i and j. In the case of the strong coupling limit with $J_H/t_{ij} \to \infty$, the effective hopping interaction t_{ij} can be expressed in terms of Anderson–Hasegawa relation [5], by neglecting the Berry phase term

$$t_{ij} = t_{ij}^0 \cos(\theta_{ij}/2). \quad (1)$$

Namely, the absolute magnitude of the effective hopping depends on the relative angle (θ_{ij}) between the neighboring (classical) spins. The ferromagnetic interaction via the exchange of the (conduction) electron is termed as the double-exchange interaction after the naming by Zener [4].

By creating electron-vacancy sites (or hole-doping) the e_g electron can hop depending on the relative configuration of the local spins. The ferromagnetic metallic state is stabilized by maximizing the kinetic energy of the conduction electrons ($\theta_{ij} = 0$). When temperature is raised up to near or above the ferromagnetic transition temperature (T_C), the configuration of the spin is dynamically disordered and accordingly the effective hopping interaction is also subject to disorder and reduced on average. This would lead to enhancement of the resistivity near and above T_C. Therefore, the large MR can be expected around T_C, since the local spins are relatively easily aligned by an external field and hence the randomness of the e_g hopping interaction is reduced. This is the intuitive explanation of the MR observed for the manganite around T_C in terms of the double-exchange (DE) model.

The physics of the colossal mangetoresistance (CMR) is obviously more complex. We will see ample examples of the failure of the simplest DE model in this article, as manifested for example by insulating behavior above T_C relevant to the CMR effect, anomolously diffusive charge dynamics even in the ferromagnetic ground state, versatile charge- and orbital-ordered states adjacent to or competitive with the DE ferromagnetic state, etc. There are certainly other important factors than in the above simplest DE scenario, which are necessary to interpret important features observed experimentally. Those are, for example, electron–lattice interaction, ferromagnetic/antiferromagnetic superexchange interaction between the local spins, intersite exchange interaction between the e_g orbitals (orbital ordering tendency), intrasite and intersite Coulomb repulsion interactions among the e_g electrons, etc. These interactions/instabilities occasionally compete with the ferromagnetic DE interaction, producing complex but intriguing electronic phases as well as the gigantic response of the system to an external field, such as CMR or the field-induced insulator–metal transition.

Among the above interactions other than the DE interaction, the important electron–lattice interaction stems from the Jahn–Teller-type coupling of the conduction e_g electrons with oxygen displacement. The Jahn–Teller interaction tends to lift the degeneracy of the d orbital and stabilize the energy level of the occupied d electrons via the deformation of metal–ligand (e.g. Mn–O) octahedron. The Mn^{3+} ($3d^4$) ion placed in the octahedral coordination is one such example, and the conduction e_g electron is subject to such a Jahn–Teller effect, spontaneously deforming the MnO_6 octahedron (see Fig. 1). In the crystal, such a Jahn–Teller distortion is collective and a coherent distortion of Mn–O network is realized, as typically seen in $LaMnO_3$ [14]. The itinerant e_g holes (or mobile Mn^{4+} species) are obviously destructive to the static distortion, yet the subsisting dynamical Jahn–Teller coupling has been argued as one of the major factors relevant to the CMR phenomena.

2.2. Perovskite structures

Most of the CMR phenomena have been found out and investigated for the manganese oxide (manganite) compounds with perovskite-type structure (Fig. 1). The perovskite-type manganites have the general formulas, $RE_{1-x}AE_xMnO_3$, where RE stands for the trivalent rare-earth element such as La, Pr, Nd, Sm, Eu, Gd, Ho, Tb,Y, etc. or for Bi^{3+}, and AE for the divalent alkaline earth ions such as Sr, Ca, and Ba or for Pb^{2+}. The (RE,AE) site (so-called perovskite A-site) can in most cases form homogeneous solid solution. Perovskite-based structures occasionally show lattice distortion as modifications from the cubic structure. One of the possible origin in the lattice distortion is the deformation of the MnO_6 octahedron arising from the Jahn–Teller effect that is inherent to the high-spin ($S = 2$) Mn^{3+} with double degeneracy of the e_g orbital. Another lattice deformation comes from the connective pattern of the MnO_6 octahedra in the perovskite structure, forming rhombohedral or orthorhombic (so-called $GdFeO_3$-type) lattice, as shown in Fig. 1 (lower panel). In those distorted perovskites, the MnO_6 octahedra show alternating buckling. Such a lattice distortion of the perovskite in the form of ABO_3 (here $A = RE_{1-x}AE_x$ and $B = Mn$ for the present manganites) is governed by the so-called tolerance factor f [15], which is defined as

$$f = (r_B + r_O)/\sqrt{2}(r_A + r_O). \quad (2)$$

Here, r_i (i = A,B (or) O) represents the (averaged) ionic size of each element. The tolerance factor f measures, by definition, the lattice-matching of the sequential AO and BO_2 planes. When f is close to 1, the cubic perovskite structure is realized. As r_A or equivalently f decreases, the lattice structure transforms to the rhombohedral ($0.96 < f < 1$) and then to the orthorhombic structure ($f < 0.96$), in which the B–O–B bond angle θ is bent and deviated from 180°. In the case of the orthorhombic lattice (see Fig. 1), the bond angle θ varies continuously with f.

The bond angle distortion decreases the one-electron bandwidth W, since the effective d electron transfer interaction between the neighboring B-sites is governed by the supertransfer process via O 2p states. For example, let us consider the hybridization between the 3d e_g state and the 2p σ state in the $GdFeO_3$ type lattice which is composed of the quasi-right BO_6 octahedra tilting alternatively. In the strong ligand field approximation, the p–d transfer interaction t_{pd} is scaled as $t^0_{pd}\cos\theta$, t^0_{pd} being for the cubic perovskite. Thus, W for the e_g electron state is approximately proportional to $\cos^2\theta$.

Another important feature in the perovskite and related structures is that the compounds are quite suitable for the carrier-doping procedure (filling control) since the structure is very robust against the chemical modification on the A-site. For example, in $La_{1-x}Ca_xMnO_3$, the solid solution can extend from $x = 0$ to 1. For AE = Sr the x can be extended up to $x = 0.7$ under normal synthetic condition, but up to $x = 1$ under high pressures. In the formula unit of $RE_{1-x}AE_xMnO_3$, the averaged Mn valence varies as $3 + x$. Namely, x produces the vacancy in the e_g electron state at a rate of x per Mn-site, and hence is referred to as the hole-doping. To be exact, the filling (n) of the e_g electron conduction band is given as $n = 1 - x$.

2.3. *Magnetoresistance of* $La_{1-x}Sr_xMnO_3$: *a canonical case*

The $La_{1-x}Sr_xMnO_3$ is the most canonical double-exchange (DE) system, since it shows the largest one-electron bandwidth W and accordingly is less significantly affected by the electron–lattice and Coulomb correlation effects. Nevertheless, the end compound $LaMnO_3$ ($x = 0$) is strongly affected by the collective Jahn–Teller effect as well as by the electron correlation effect due to the $n = 1$ filling of the e_g band. The collective Jahn–Teller distortion present in $LaMnO_3$ reflects the orbital ordering such as the alternating $d_{3x^2-r^2}$ and $d_{3y^2-r^2}$ orbitals on the *ab* plane [14]. In this Jahn–Teller-distorted and orbital-ordered state, the $LaMnO_3$ undergoes the antiferromagnetic transition at 120 K. The spin-ordering structure is layer type or so-called A-type, in which the ferromagnetic *ab* plane is coupled antiferromagnetically along the *c*-axis.

With the hole-doping by substitution of La with Sr, the ordered spins are canted toward the *c*-axis direction. In the pioneering paper by Wollan and Koehler for $La_{1-x}Ca_xMnO_3$ [16], they argued the spin state in such a lightly doped region in terms of the mixture of the ferromagnetic and antiferromagnetic domains. This was however reinterpreted in terms of the DE mechanism by de Gennes [6]: The extension of the wave function of the hole along the *c*-axis can mediate the DE-type ferromagnetic coupling, producing the spin canting. (This problem, namely the spin canting vs. the two-phase coexistence, has recently been revived in the light of theoretical views on the generic phase separation instability in correlated electron systems, but here for explanation of the phase diagram, we tentatively follow the de Gennes's interpretation.) As the doping level x increases, the spin canting angle is continuously increased to the nearly ferromagnetic spin structure. In $La_{1-x}Sr_xMnO_3$ [17,18], the canted antiferromagnetic phase appears to persist up to $x = 0.15$, although for $x > 0.10$ the spin-ordered phase is almost ferromagnetic. With further doping, the ferromagnetic phase appears below T_C which steeply increases with x up to 0.3 and then saturates. Another important consequence of the hole-doping is that the static collective Jahn–Teller distortion present in $LaMnO_3$ is diminished with increase of the doping level, perhaps beyond $x = 0.10$. This is manifested by the structural transformation between two types of orthorhombic forms [18].

The temperature dependence of resistivity and the magnetic field effect are exemplified in Fig. 2 (left panel) for the $x = 0.175$ crystal [11,17]. The resistivity shows a steep decrease around T_C (indicated by an arrow), indicating that the relatively high resistivity above T_C is dominantly due to the scattering of the conduction electrons by thermally disordered spins. The magnetic field greatly reduces the resistivity near T_C due to the suppression of the spin-scattering of the e_g-state carriers. Such a negative magentoresistance (MR) is nearly isotropic with respect to the direction of the applied field. The MR value defined as $-[\rho(H) - \rho(0)]/\rho(0)$ is also plotted in Fig. 2 by open circles at a field of $\mu_0 H = 15$ T.

Fig. 2 (right) shows the correlation between the field-induced changes in ρ and M for the $x = 0.175$ crystal. The magnitude of the MR correlates with the change in M; the MR is large around T_C, but very small at temperatures (e.g., 78 K for $x = 0.175$) far below T_C. The rapid rise of the M–H curve in the low-temperature ferromagnetic phase is due to the domain rotation in the present soft ferromagnet, which appears to least affect the ρ value.

The resistivity change thus appears to be scaled with the change of the magnetization of the system. With use of the M–H and ρ–H curves at respective temperatures, the change of the resistivity can be deduced as a function of M. The result for an $x = 0.175$ crystal is shown in Fig. 3 [11,17]. Looking at this ρ–M curve, one may notice that the experimental points taken at different temperatures above T_C show an approximately identical curve in spite of seemingly different MR behaviors. In Fig. 3 is also shown the ρ–M curve which was obtained by the temperature dependence of the ρ and M data taken at a field of 0.5 T. The curve shows a similar trace to the universal curve obtained from the field dependence. The good coincidence suggests that the ρ–T curve is also governed by a similar scattering process to the case of the MR. The experimental points taken below T_C draw horizontal lines (dashed lines) in the low-M region, but merge to the

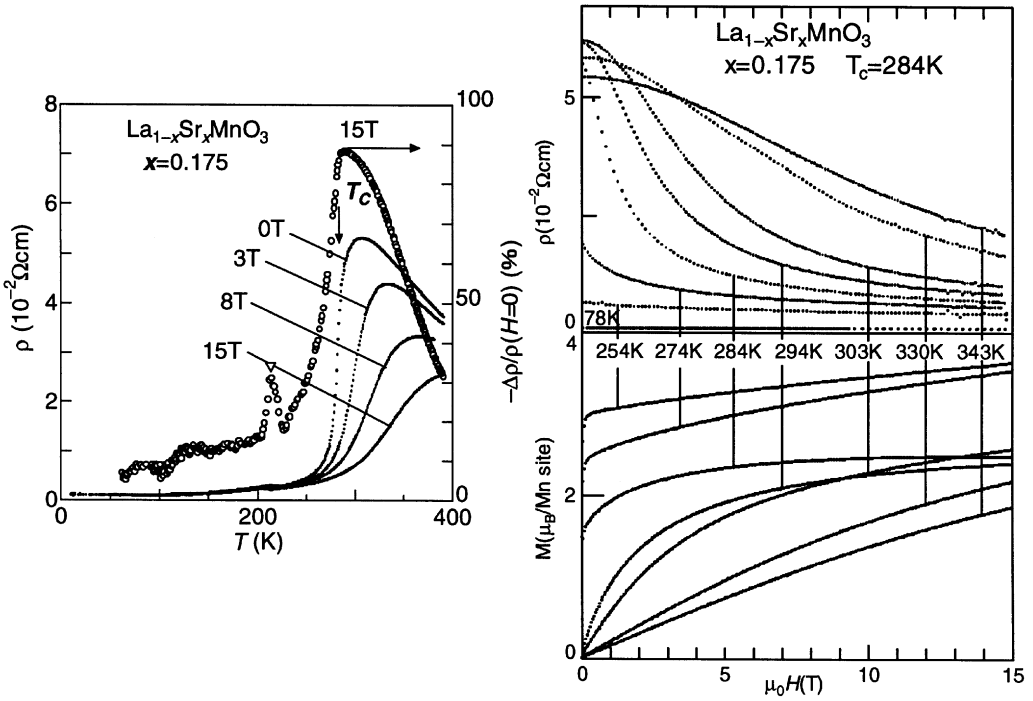

Fig. 2. Left: Temperature dependence of resistivity for a $La_{1-x}Sr_xMnO_3$ ($x = 0.175$) crystal at various magnetic fields. Open circles represent the magnitude of negative magnetoresistance $-[\rho(H) - \rho(0)]/\rho(0)$ with a magnetic field of 15 T. Right: The resistivity (upper panel) and magnetization (lower panel) as a function of magnetic field for a $La_{1-x}Sr_xMnO_3$ ($x = 0.175$) crystal.

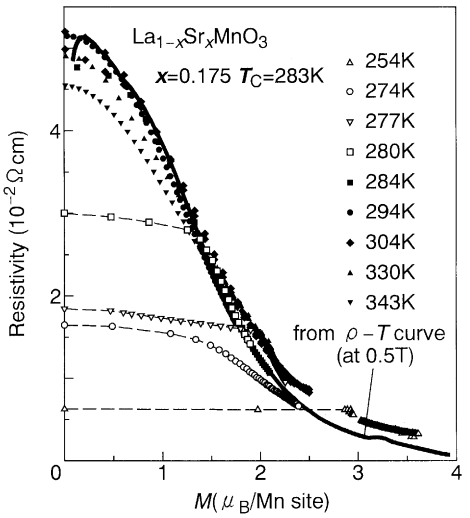

Fig. 3. Change of the resistivity as a function of magnetization for a $La_{1-x}Sr_xMnO_3$ crystal ($x = 0.175$). The points are obtained from the ρ–H and M–H curves at respective temperatures. The solid line is obtained using the ρ–T and M–T curves with a field of 0.5 T.

universal curve in the high-M region. The initial magnetization is governed by the domain rotation (typically below 0.2 T) and does not influence the carrier-scattering process. A small but systematic discrepancy between the temperature- and field-variation curves in the high-M region is ascribed to the temperature-dependent scattering process other than the simple spin scattering.

The observed MR features near T_C for $La_{1-x}Sr_xMnO_3$ are viewed as canonical for the DE system, and the M dependence of the MR value at a temperature near above T_C is well expressed by a scaling function

$$-[\rho(H) - \rho(0)]/\rho(0) = C(M/M_s)^2, \quad (4)$$

at least in the relatively low-M region, say $M \leqslant 0.3M_s$ (M_s is the saturation magnetization in the ground state). The scaling constant C remarkably depends on the doping level x: The C is as high as 4 near the metal–insulator phase boundary ($x = 0.175$) but steeply decreases with x and

becomes ≈ 1 at $x = 0.4$. The scaling constant C measures the effective coupling between the e_g conduction electron and the t_{2g} local spin. In terms of the simple DE model, the coupling is dominated by the quantity J_H/W and x, W being the one-electron bandwidth of the e_g conduction band. According to the dynamical mean-field theory of the DE model [19], the C can be as large as 4 in the case of the strong coupling, namely $J_H/W \gg 1$, but become 1 in the weak coupling limit. Furthermore, other competing interactions with the DE interaction can enhance the resistivity above T_C and resultantly cause the larger MR, producing the seemingly very large C value (> 4). The hole-doping dependence of C indicates that the increase of the nominal hole concentration x drives the system effectively towards the weak coupling regime.

Concerning the empirical expression for the M-dependence of the resistivity (ρ), Hundley et al. [20] proposed a more general formula that fits a broader temperature and field region,

$$\rho(H, T) = \rho_m \exp[-M(H, T)/M_0], \quad (5)$$

where M_0 is a scaling parameter with dimension of magnetization. If the polaron hopping type transport is relevant near T_C, it should be activated by the effective hopping interaction t_{eff}, namely, $\rho \propto \exp(-t_{eff})$. With $t_{eff} \propto M$, Eq. (5) suggests that polaronic hopping is the prevalent conduction mechanism near below T_C.

An important issue directly relating to the CMR effect is a semiconducting or insulating behavior above T_C in the rather low-x region, e.g. $x = 0.15$–0.20 of $La_{1-x}Sr_xMnO_3$ or in narrower-W systems such as $La_{1-x}Ca_xMnO_3$. In such an x region, the negative MR effect is most pronounced around T_C and hence the origin of the semiconducting transport is of great interest. Millis et al. [21] pointed out that the resistivity of the low-doped crystals above T_C is too high to be interpreted in terms of the simple DE model and ascribed its origin to the dynamic Jahn–Teller distortion. The static and coherent Jahn–Teller distortions disappear above $x = 0.1$ in $La_{1-x}Sr_xMnO_3$, judging from the crystal-structural phase change between the two orthorhombic forms [18]. However, Jahn–Teller coupling energy is large (an order of 1 eV) and should remain finite when the carrier mobility is reduced by disordered spin configuration above T_C. Therefore, the mean amplitude of the Jahn–Teller distortion is critically reduced in lowering temperature below T_C, as theoretically demonstrated by Millis et al. [22]. This is also considered as a consequence of the crossover from small polaron to large polaron with decreasing temperature through T_C or applying a magnetic field near T_C [23]. In fact, the presence of the dynamic Jahn–Teller distortion has been evidenced in some experiments, in particular for a narrower bandwidth system, $La_{1-x}Ca_xMnO_3$ [24,25]. Thus, the tunable electron–lattice coupling or temperature- and magnetic field-dependent formation of Jahn–Teller polarons is an important feature of the CMR manganites.

Another possible origin of the resistivity increase near above T_C and the effective suppression by an external magnetic field has been ascribed to the Anderson localization of the DE carriers arising from the inevitably present random potential in the solid solution system [26], or to antiferromagnetic spin fluctuation which competes with the DE interaction [27,28]. An important issue relating to these instabilities is how we can take into account the orbital degree of the freedom of the e_g-state electrons and their possible strong intersite correlation or coupling to the lattice degree of freedom. We will later come back to this problem, taking example of more conspicuous cases.

2.4. Ferromagnetic ground state

In addition to the large MR effect around T_C, the low-temperature ferromagnetic metallic state in a prototypical DE system, $La_{1-x}Sr_xMnO_3$, is also unique and important from the following viewpoints: (1) the Mott transition induced by the change of the doping level (x) or the band filling ($n = 1 - x$), and (2) dynamics of charge carriers with nearly full spin polarization but with orbital degeneracy inherent to the e_g state. The former view is based on the assumption that the origin of the charge gap in the parent insulator $LaMnO_3$ is dominantly due to the electron correlation, namely the on-site Coulomb interaction of e_g conduction electrons. In the conventional-doped Mott

insulators (including both Mott–Hubbard or charge-transfer insulators), such as high-temperature superconducting cuprate compounds, the metallic state near the insulator-metal (or Mott) transition is subject to strong antiferromagnetic spin fluctuation. By contrast, the doping-induced metallic ground state, e.g., in $La_{1-x}Sr_xMnO_3$, is fully spin-polarized (half-metallic) with no spin degree of freedom left at zero temperature. This may signal that the Mott transition in $La_{1-x}Sr_xMnO_3$ or the barely metallic state may differ qualitatively from the conventional carrier-doped (filling-controlled) Mott insulators.

On the other hand, the orbital-ordered state with $3x^2 - r^2$ and $3y^2 - r^2$ as seen in the parent compound $LaMnO_3$ appears to subsist against hole doping up to $x = 0.1$, above which the ferromagnetic state emerges (see also Fig. 6). If the orbital degree of freedom is viewed as pseudo-spin [29,30], then such an "antiferromagnetic (C-type)" orbital ordering is quantum-melted by doping of mobile holes. This is quite analogous to the doped antiferromagnetic Mott insulator where the mobile holes lead to the collapse of the spin-ordered state and produce the correlated metallic state. Likewise, the barely metallic ground state in the fairly low-doped region may show the pseudo-spin moment arising from the orbital degree of freedom and its transport properties be affected by the orbital correlation/fluctuation. If the Jahn–Teller coupling between the orbital and lattice degrees of freedom is appreciable, the dynamic and cooperative Jahn–Teller distortion may be present even in the metallic ground state. In fact, quasi-elastic neutron diffraction studies probing the pair distribution function (PDF) [31] as well as phonon Raman scattering studies [32] have indicated the presence of the Jahn–Teller distortion or large (or medium-size) polarons even in the low-temperature metallic state. In spite of this conjecture and some supporting experimental evidences, the detailed aspects of the ferromagnetic ground state suffering from strong orbital fluctuations or accompanying lattice dynamics are still left to be explored.

In Fig. 4 is plotted the doping(x)-dependence of the inverse of residual resistivity, the Hall coefficient R_H, the electronic specific heat constant γ, and the lattice Debye temperature Θ_D in the vicinity

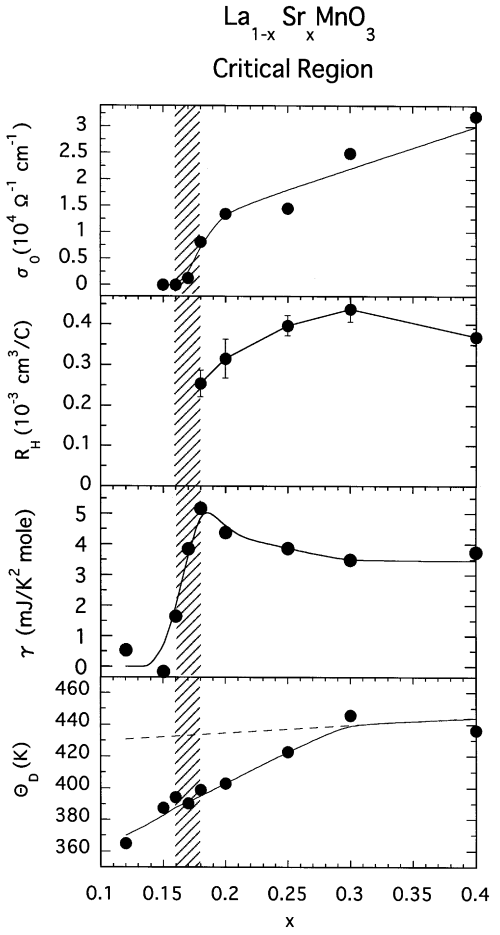

Fig. 4. Doping level x dependence of zero-temperature conductivity σ_0 (inverse of residual resistivity), Hall coefficient R_H, electronic specific heat coefficient γ, and Debye temperature Θ_D, for $La_{1-x}Sr_xMnO_3$ crystals. A hatched vertical bar indicates the metal-insulator transitional region, where the resistivity up-turn is observed at a lower temperature than T_C (Curie temperature).

of the metal-insulator transition ($x_c = 0.16$) of $La_{1-x}Sr_xMnO_3$ [33]. The hatched region represents the MI transitional region where the resistivity shows up-turn at lower temperatures below T_C, where some ordering in charge and/or orbital sectors is likely to occur [34,35]. The specific heat at low temperatures in $La_{1-x}Sr_xMnO_3$ crystals [33,36] is composed of the three components; lattice T^3-term (Θ_D^3), spin-wave $T^{3/2}$-term, and T-liner electronic part. The figure shows the electronic part γ and the lattice term (Θ_D). The third panel of the figure represents the ordinary part of Hall effect

observed at 4.2 K. In such a low-temperature region, the contribution from the anomalous Hall effect characteristic of the ferromagnetic metal is negligible [37]. Over the whole metallic region ($x > 0.18$), the Hall coefficient takes a positive small value (indicating nominally ≈ 1 hole per Mn site) which is characteristic of a metal with a large Fermi surface. In other words, the Fermi surface retains its area down to near the metal–insulator phase boundary even in the presence of the aforementioned dynamical (and perhaps collective) Jahn–Teller distortion.

The γ value, which represents the density of state at the Fermi level in the case of a conventional metal, shows a minimal enhancement even near the metal–insulator boundary and steeply decreases to zero in the transitional region in between $x = 0.18$ and 0.15. This is in contrast with the canonical cases of the doping-induced Mott transition in strongly correlated electron systems, such as V_2O_3 [38,39] and $LaTiO_3$ [40,41], in which the critical enhancement of γ or the strong mass renormalization effect is observed in common near the metal–insulator phase boundary. The residual resistivity, which should be irrelevant to the electron correlation (Coulomb interaction), shows a large reduction with the increase of x from 0.18 (see the top panel of Fig. 14) and also under pressures [42].

Such a diffuse charge dynamics may originate from the aforementioned orbital fluctuations or the Jahn–Teller type electron-lattice coupling. However, the identity of the carriers is not a conventional small polaron, since no mass enhancement is observed even in the vicinity of the metal-insulator boundary. However, some lattice anomaly manifests itself in the anomalous x-dependence of Debye temperature Θ_D, as shown in the bottom panel of Fig. 4. A dashed line is a reference that is expected from the slight change of material density. Thus, it is clear that anomalous softening of the lattice occurs below $x = 0.3$, which are not apparently relevant to the orthorombic-rhombohedral structural transition taking place around $x = 0.2$ nor to the metal-insulator phase boundary. The orbital ordering of the $3x^2 - r^2$ and $3y^2 - r^2$ as observed in the $LaMnO_3$ is melted above $x = 0.10$, yet such an apparent softening of lattice in between $x = 0.1$ and 0.3 [33,36] is likely due to the Jahn–Teller-type lattice distortion which is dynamical and short-range ordered.

Another distinct experimental indication against the picture of a simple half-metallic ground state is the anomalously incoherent feature of the charge dynamics as seen in the optical conductivity spectra. The temperature dependence of spectra of the optical conductivity for a $La_{1-x}Sr_xMnO_3$ ($x = 0.18$) crystal is shown in Fig. 5. As seen in this figure, the gap-like transition on the higher-energy (>1 eV) side gradually decreases in intensity with the decrease of temperature, while the spectral weight of the lower-lying (<1 eV) band increases. These two types of transitions, between which the spectral intensity is exchanged depending on the spin polarization, can be explained by the crossover from the interband transition between the exchange-split e_g -bands to the intraband transition within the e_g-conduction band [43,44]. The low-energy spectra are composed of the nearly ω-independent incoherent part and the sharply $\omega = 0$ centered Drude response, as shown in the inset of Fig. 5. Even the ground-state spectrum is, however, dominated by the incoherent component concerning the spectral weight. In fact, the estimated Drude

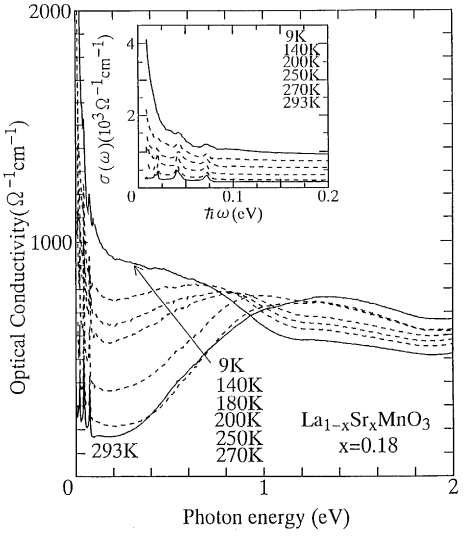

Fig. 5. Temperature dependence of optical conductivity spectra of a $La_{1-x}Sr_xMnO_3$ ($x = 0.180$) crystal. The inset shows the magnification below 0.2 eV.

weight is extremely small (0.02–0.03 as effective number of electrons, N_{eff}). This can neither be ascribed to heavy effective mass nor small carrier density as compared with the results of the Hall coefficient and specific heat in Fig. 4. Thus, the conventional Drude model is not applicable to the ferromagnetic metallic state in $La_{1-x}Sr_xMnO_3$ where the carrier motion is mostly incoherent. The strong scattering in the fully spin-polarized ground state without any appreciable mass renormalization may be ascribed to the orbital degree of freedom in the e_g state, as theoretically argued [45,46], or otherwise to dynamical phase segregation [47] composed of the ferromagnetic–metallic (double-exchange-mediated) and ferromagnetic–insulating (orbital-ordered super-exchange-mediated) states. The problem is of current interest and yet to be settled.

3. Compositional tuning of CMR and its implication in the CMR mechanism

3.1. Variation of electronic phase diagrams

We show in Fig. 6 electronic phase diagrams in the temperature (T) vs. hole concentration (x) plane for prototypical compounds [48]; (a) $La_{1-x}Sr_xMnO_3$, (b) $Nd_{1-x}Sr_xMnO_3$ and (c) $Pr_{1-x}Ca_xMnO_3$. As the tolerance factor or equivalently the averaged ionic radius of the perovskite A-site decreases from (La,Sr) to (Pr,Ca) through (Nd,Sr), the orthorhombic distortion of $GdFeO_3$-type increases, resulting in the bending of the Mn–O–Mn bond and hence in the decrease of the one-electron bandwidth (W) of the e_g-state carriers. This means that other electronic instabilities, such as the charge/orbital-ordering and super-exchange interactions which compete with the double-exchange (DE) interaction, may become dominant in specific regions of x and temperature.

The phase diagram for $La_{1-x}Sr_xMnO_3$ with maximal W is canonical as the DE system, as described in the former section. The decrease of W complicates the phase diagram. In particular, when the doping x is close to the commensurate value $x = 1/2$, the charge-ordering instability comes to the surface. In the case of $Nd_{1-x}Sr_xMnO_3$ (Fig. 6), the ferromagnetic metallic (FM) phase shows up for $x > 0.3$, yet in the immediate vicinity of $x = 1/2$ the FM state changes into the charge-ordered insulating (COI) state with decrease of temperature below $T_{CO} = 160$ K. This COI state

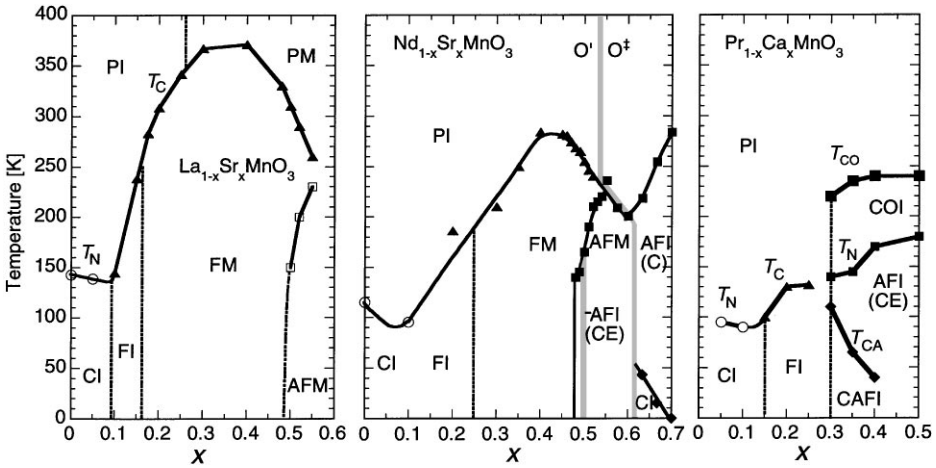

Fig. 6. The magnetic as well as electronic phase diagrams of $La_{1-x}Sr_xMnO_3$ (left), $Nd_{1-x}Sr_xMnO_3$ (middle) and $Pr_{1-x}Ca_xMnO_3$ (right). The PI, PM and CI denote the paramagnetic insulating, paramagnetic metallic and spin-canted insulating states, respectively. The FI,FM, and AFM denote the ferromagnetic insulating and ferromagnetic metallic, and antiferromagnetic (A-type) metallic states, respectively. At $x = 0.5$ in $Nd_{1-x}Sr_xMnO_3$, the charge-ordered insulating (COI) phase with CE-type spin ordering is present. For $0.3 \leqslant x \leqslant 0.5$ in $Pr_{1-x}Ca_xMnO_3$, the antiferromagnetic insulating (AFI) state exists in the charge-ordered insulating (COI) phase. The canted antiferromagnetic insulating (CAFI) state also shows up below the AFI state in the COI phase for $0.3 \leqslant x \leqslant 0.4$.

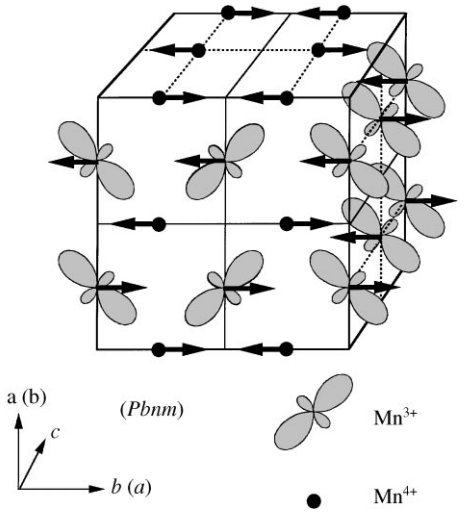

Fig. 7. Spin, charge, and orbital ordering pattern of the CE type observed for most of the $x \approx 1/2$ manganites. The e_g-orbital ordering on Mn^{3+} sites are also shown. The Mn^{4+} sites are indicated by closed circles.

accompanies the concomitant antiferromagnetic ordering of orbitals and spins, that is so-called CE type [16,49–51], as shown in Fig. 7. The nominal Mn^{3+} and Mn^{4+} species with a 1 : 1 ratio shows a real-space ordering on the (001) plane of the orthorhombic lattice (P_{bnm}), while the e_g orbital shows the 1×2 superlattice on the same (0 0 1) plane. Reflecting such an orbital ordering, the ordered spins form a complicated sublattice structure extending over a larger unit cell as shown in the figure. Although a similar concomitant charge- and spin-ordering is widely seen in 3d electron transition metal oxides [13], the most notable feature of the manganites is the magnetic-field-induced melting of the CO state, which shows up as the field-induced phase transition from an antiferromagnetic insulator to a ferromagnetic metal [52].

With the hole concentration of $x > 0.52$, the A-type (layer-type) AF ordering turns up again [53–55]. As evidenced by the change in lattice parameters toward the A-type AF phase (i.e., the a, b-axes expanding and the c-axis shrinking), the uniform ordering of $d_{x^2-y^2}$ orbitals appears to be realized in the A-type AF phase in such an overdoped region ($0.52 < x < 0.62$). Note the difference of the orbital ordering in the present overdoped metallic manganites $RE_{1-x}Sr_xMnO_3$ (RE = La, Pr, and Nd; $0.5 < x < 0.6$) and the insulating parent material $REMnO_3$ ($x = 0$), in the latter of which the same A-type AF structure appears with the orbital ordering of $3_{x^2-r^2}$ and $3_{y^2-r^2}$ on the ab plane. The uniform ordering of $x^2 - y^2$ orbitals makes the phase metallic but 2D-like as observed ($\sigma_{ab}/\sigma_c \approx 10^4$ at 35 mK) [54], since the inter-plane (c-axis) hopping of the fully spin-polarized $d_{x^2-y^2}$ electron is almost forbidden due to the in-plane confinement in the layered-AF structure as well as to the minimal supertransfer interaction between the $x^2 - y^2$ orbitals along the z-direction. The mean-field theory for electronic phase diagram of pseudo-cubic manganites also predicts that the layered A-type AF state near $x = 0.5$ accompanies the $x^2 - y^2$ orbital-ordering [56]. As x is further increased, the rod type (C-type) AF ordering turns up at $x > 0.62$ (Fig. 6). As evidenced by the elongation of a lattice parameter along the c-axis, the $3z^2 - r^2$ orbitals are mostly occupied in the C-type AF phase.

For $Pr_{1-x}Ca_xMnO_3$ with a further reduced tolerance factor, the CO phase is present below 220–240 K for $x \geqslant 0.3$ and no FM phase shows up in any x-region at zero field. In the CO phase of this compound, there are successive magnetic transitions to the CO antiferromagnetic insulating (AFI) phase and to the CO spin-canted insulating (CAFI) phase [50,51,57,58]. An observed variation of the transition temperatures T_N and T_{CA} with x can be interpreted in terms of the partial revival of the DE carriers in the CO phase [59]: The CO pattern is always (π,π,0) in the pseudo-cubic setting irrespective of x and hence the deviation of x from $x = 0.5$ may produce extra carriers which mediate the DE interaction along the c-axis and play a role of modifying the antiferromagnetic spin structure towards the ferromagnetic one, as observed. Such a discommensuration of the nominal hole concentration seems to affect not only the temperature-dependent spin structure but also the metal-insulator phase diagram in the T–H plane (see Section 4.2).

3.2. Compositional tuning of CMR

The ferromagnetic transition temperature T_C is a good measure for the kinetic energy of the

double-exchange (DE) carriers, which would scale linearly with the e_g electron hopping interaction or the conduction bandwidth (W) in the case of the simple DE ferromagnet. The T_C in the perovskite manganties, $RE_{1-x}Sr_xMnO_3$ (RE = La, Pr, Nd, Sm and their solid solution), are in fact very sensitive to the doping level and the tolerance factor (degree of lattice distortion) which are both closely relevant to the carrier kinetic energy [59,60]. Fig. 8 shows the T_C for various doping (x) levels as a function of the tolerance factor f, defined by Eq. (2) [60]. The temperature of the charge ordering transition is also indicated for the $x = 0.5$ crystals. The ferromagnetic transition temperature T_C decreases with decease in f or W irrespective of x. In particular, the rate of the reduction in T_C is enhanced below some critical value of f (~ 0.975 for $x = 0.5$, ~ 0.970 for $x = 0.45$, and ~ 0.964 for $x = 0.4$).

Let us first see the case of $x = 0.5$. For $f > 0.976$ (RE = Nd) the T_C is almost constant and the charge-ordered state exists at lower temperatures (see the curves for $Nd_{0.5}Sr_{0.5}MnO_3$ in Fig. 8). For $f < 0.976$, however, the reduction of T_C with decrease of f is pronounced. Since the T_C should depend almost linearly on the W (and hence f in this region) in the simple DE model, such a pronounced suppression of T_C suggests that other instabilities which compete with the DE interaction become important for $f < 0.976$. In this region, the hysteresis (first-order nature) of the ferromagnetic transition and the deviation of the inverse susceptibility from the Curie–Weiss law are also pronounced [60]. For $f < 0.971$, the ferromagnetic metallic state disappears and in turn the charge-ordered state is present below some critical temperature, e.g., $T_{CO} = 230$ K for $Pr_{1/2}Ca_{1/2}MnO_3$ (see also Figs. 6 and 11).

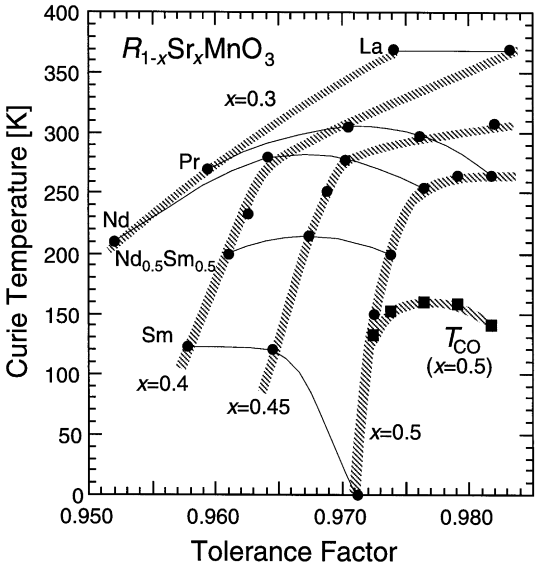

Fig. 8. The critical temperatures of the ferromagnetic transition (solid circles) and the charge-ordering transition for $x = 0.5$ (solid squares) in $RE_{1-x}Sr_xMnO_3$ (RE = La, Pr, Nd, Sm and their solid solution) crystals as a function of the tolerance factor. The tolerance factor (f) is defined as $f = (r_A + r_O)/\sqrt{2}(r_B + r_O)$ where r_A, r_B and r_O are ionic radii of the perovskite A, B (Mn) site cations and oxygen, respectively. The hatched thick lines and the solid thin ones are the guides to the eye, connecting the identical x and RE compounds, respectively.

In Fig. 8, similar suppression in T_C is seen also for $f < 0.970$ in $x = 0.45$ and for $f < 0.964$ in $x = 0.4$, although no (long-range) charge-ordered state is present even at low temperatures. In such a f-region as showing anomalously low T_C, the restoration of the DE interaction by the magnetic field is most conspicuous and hence the magnetoresistance around T_C is maximized, as shown in the following. We compare the cases of $Sm_{1-x}Sr_xMnO_3$ and $Nd_{1-x}Sr_xMnO_3$ ($x = 0.45$) with a small difference in the tolerance factor but with a big difference in T_C. Fig. 9 shows the temperature dependence of resistvitiy under various magnetic fields for the both crystals [60]. The MR is seen around the T_C in the both crystals, but the magnitude differs significantly for the $Nd_{1-x}Sr_xMnO_3$ ($x = 0.45$) and $Sm_{1-x}Sr_xMnO_3$ ($x = 0.45$) crystals: The latter crystal shows a gigantic decrease of resistivity by four orders of magnitude at T_C and the above-T_C resistivity is likewise reduced by application of fields, while the former crystal shows a rather canonical behavior of MR, being similar to that of $La_{1-x}Sr_xMnO_3$ with maximal W. The upper panel of Fig. 9 shows the Curie–Weiss plot (H/M vs. T) for the both crystals measured at 0.5 T. The Weiss temperature of $Nd_{1-x}Sr_xMnO_3$ ($x = 0.45$) coincides with the T_C, whereas the H/M for $Sm_{1-x}Sr_xMnO_3$ ($x = 0.45$) shows a deviation from the simple Curie-Weiss behavior below about 230 K and at T_C the magnetic state is suddenly switched to the

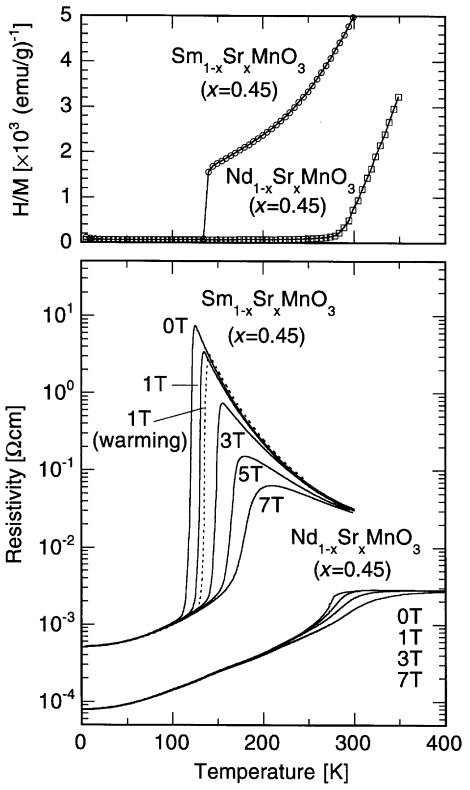

Fig. 9. The temperature dependence of resistivity under several magnetic fields for crystals of $Nd_{1-x}Sr_xMnO_3$ ($x = 0.45$) and $Sm_{1-x}Sr_xMnO_3$ ($x = 0.45$). The dashed line for $Sm_{1-x}Sr_xMnO_3$ ($x = 0.45$) indicates the warming run at 1 T. Upper panel shows the Curie–Weiss plot for the respective compounds, whose magnetization was measured at 0.5 T.

ferromagnetic one. The anomalous increase of resistivity above T_C (and its critical field suppression) for $Sm_{1-x}Sr_xMnO$ ($x = 0.45$) must be relevant to such an antiferromagnetic interaction competing with the ferromagnetic DE interaction.

Furthermore, large lattice-structural change or anisotropic strain upon the ferromagnetic transition as well as the gigantic magnetostriction is observed for $Sm_{1-x}Sr_xMnO_3$ ($x = 0.45$), but much less for $Nd_{1-x}Sr_xMnO_3$ ($x = 0.45$) [60]. The observed distinctive features for the both crystals, $Nd_{1-x}Sr_xMnO_3$ ($x = 0.45$) and $Sm_{1-x}Sr_xMnO_3$ ($x = 0.45$), indicate that the colossal feature of the MR is obviously relevant to the switching of the magnetism above T_C as well as of the lattice strain. The anisotropic feature of the magentostriction coupled to the gigantic MR for the $Sm_{1-x}Sr_xMnO_3$ ($x = 0.45$) crystal implies that the relevant dynamical Jahn–Teller distortions are strongly spatially correlated. Such a collective nature of the Jahn–Teller distortion above T_C likely arises from the anisotropic short-range orbital ordering or fluctuation. In particular, the e_g orbitals are already aligned perpendicular to the c-axis and show the directional order (i.e., with little $3z^2 - r^2$ component), while the in-plane ordering remains short-ranged. The situation may be viewed as a "liquid-crystal" state (like nematic phase) for the orbital degree of freedom.

4. Magnetic field induced melting of charge/orbital ordered states

4.1. Charge/orbital ordering at $x = 1/2$

In Fig. 10 are shown typical examples of the charge/orbital ordering transitions observed for $Nd_{1-x}Sr_xMnO_3$ ($x = 0.5$) [61] and $Sm_{1-x}Ca_xMnO_3$ ($x = 0.5$) [62]. As shown in the temperature dependencies of resistivity and magnetization, the charge/orbital ordering transitions manifest themselves as decrease in magnetization and increase in resistivity, which locate at $T_{CO}(= T_N) \approx 160$ K in $Nd_{1/2}Sr_{1/2}MnO_3$ (left) and $T_{CO} \approx 270$ K in $Sm_{1/2}Ca_{1/2}MnO_3$ (right), respectively. Changes in lattice parameters are also observed at T_{CO}; elongation in the orthorhombic a- and b-axes and contraction in the c-axis, which suggests that ordering of e_g-orbital occurs simultaneously. Such a change in lattice parameters upon the charge/orbital ordering transition as shown in Fig. 10 has also been reported for polycrystalline $La_{1/2}Ca_{1/2}MnO_3$ ($T_{CO}(= T_N) \approx 160$ K) [63,64]. In $Nd_{1/2}Sr_{1/2}MnO_3$, the ferromagnetic and metallic state due to the double-exchange (DE) interaction is seen below $T_C \approx 255$ K, and subsequently the transition to the antiferromagnetic charge/orbital-ordered state occurs at $T_{CO}(= T_N) \approx 160$ K [61]. In $Sm_{1/2}Ca_{1/2}MnO_3$, similar changes in resistivity and magnetization are seen at $T_{CO} \approx 270$ K [62], where the charge/orbital ordering takes place.

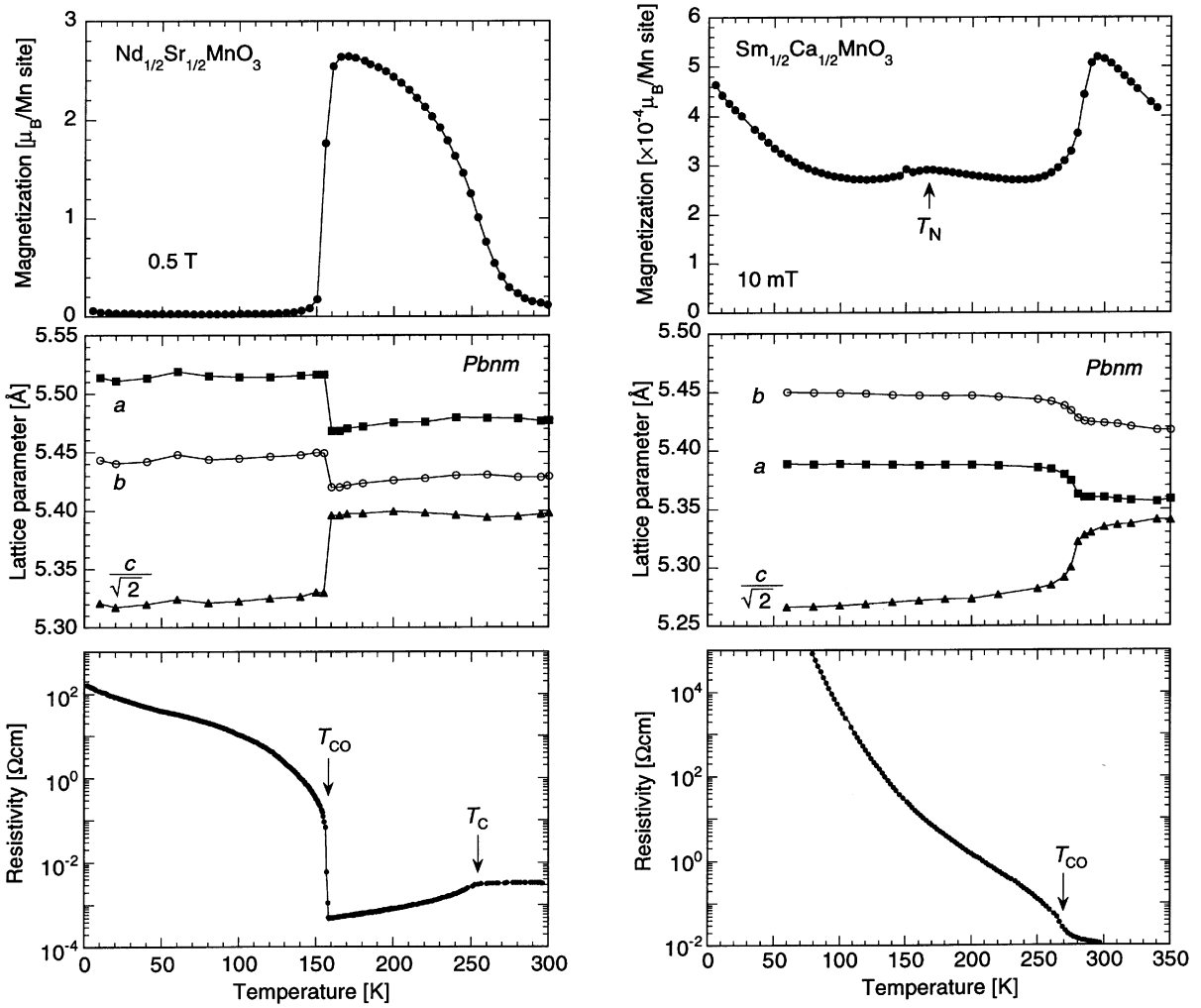

Fig. 10. The temperature dependencies of magnetization (top), resistivity (middle) and lattice parameters (bottom) observed for $Nd_{1/2}Sr_{1/2}MnO_3$ (left) and $Sm_{1/2}Ca_{1/2}MnO_3$ (right). In $Nd_{1/2}Sr_{1/2}MnO_3$ the critical temperature of the charge/orbital ordering transition coincides with the antiferromagnetic Nèel temperature ($T_{CO} = T_N \approx 160$ K), while in $Sm_{1/2}Ca_{1/2}MnO_3$ the former is higher than the latter ($T_{CO} \approx 270$ K and $T_N \approx 170$ K).

As is clear from the temperature dependence of magnetization, however, the antiferromagnetic spin-ordering occurs not concurrently but at a lower temperature, $T_N \approx 170$ K, and no ferromagnetic state is present at zero field. In the reduced-bandwidth systems, such as $RE_{1/2}Ca_{1/2}MnO_3$(RE = Pr, Nd, Sm, ...), in which no ferromagnetic or metallic state is realized, a split between T_{CO} and T_N is generally observed. A similar feature is also observed for the related material with the layered-perovskite structure, $La_{1-x}Sr_{1+x}MnO_4(x = 1/2)$, where $T_{CO} \approx 217$ K and $T_N \approx 110$ K [65].

In $Nd_{1/2}Sr_{1/2}MnO_3$, an antiferromagnetic spin ordering of the CE-type (Fig. 7) with the magnetic unit cell expanding to $2 \times 2 \times 1$ of the original orthorhombic lattice has been confirmed below T_{CO} by a neutron diffraction study [53]. In

$Sm_{1/2}Ca_{1/2}MnO_3$ the charge/orbital- and spin-ordering as shown in Fig. 7 are realized below T_N. The charge/orbital ordering at $x = 1/2$ is thus characterized by the antiferromagnetic CE-type structure which has originally been revealed for $La_{1-x}Ca_xMnO_3$ ($x \approx 1/2$) [16].

In the magnetization curve for the charge/orbital ordered state, we can see the metamagnetic transition. In accord with this, the resistivity also shows steep decrease by several orders of magnitude. Thus, the transition from the antiferromagnetic charge/orbital-ordered insulating state to the ferromagnetic metallic one is caused by application of an external magnetic field. From a thermodynamic point of view, the both states are energetically almost degenerate, but the free energy of the ferromagnetic (FM) state can be decreased by the Zeeman energy $-M_sH$ (M_s, the spontaneous magnetization) so that the magnetic field-induced transition to the FM metallic state takes place in an external magnetic field.

Fig. 11 shows the charge/orbital ordering phase diagrams for various $RE_{1/2}AE_{1/2}MnO_3$ crystals which are presented on the magnetic field–temperature (H–T) plane. The phase boundaries have been determined by the measurements of the magnetic field dependence of resistivity (ρ–H) and magnetization (M–H) at fixed temperatures [61,66], and those for $RE_{1/2}Ca_{1/2}MnO_3$ (RE = Pr, Nd and Sm) have been obtained by measurements utilizing pulsed high magnetic fields up to 40 T [67]. In this figure, the critical field to destruct the charge/orbital-ordered state in $Nd_{1/2}Sr_{1/2}MnO_3$ is about 11 T at 4.2 K, while that in $Pr_{1/2}Ca_{1/2}MnO_3$ increases to about 27 T. In the case of $Sm_{1/2}Ca_{1/2}MnO_3$, the charge/orbital ordering is so strong that the critical field becomes as large as about 50 T at 4.2 K. Fig. 11 thus demonstrates that the robustness of the charge/orbital ordering at $x = 1/2$ critically depends on the W, which is understood as a competition between the DE interaction and the ordering of Mn^{3+}/Mn^{4+} with a 1 : 1 ratio accompanied by simultaneous ordering of e_g-orbital of Mn^{3+}.

To be further noted in Fig. 11 is the large hysteresis of the transition (hatched in the figure) which is

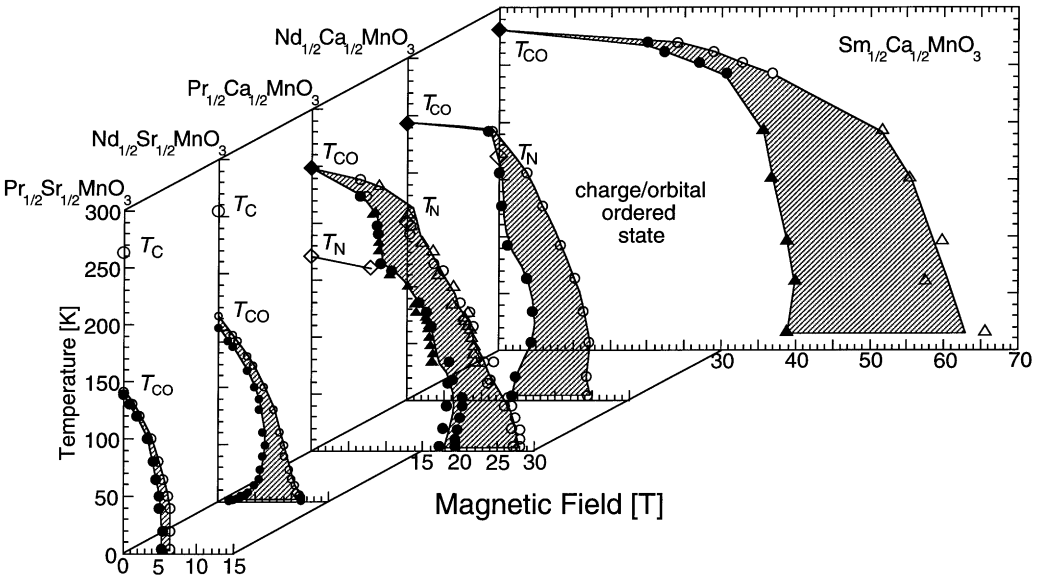

Fig. 11. The charge/orbital-ordered phase of various $RE_{1/2}AE_{1/2}MnO_3$ plotted on the magnetic field-temperature plane. The phase boundaries have been determined by measurements of the magnetic field dependence of resistivity (ρ–H) and magnetization (M–H) at fixed temperatures [61,66], and those for $RE_{1/2}Ca_{1/2}MnO_3$ (RE = Pr, Nd and Sm) have been obtained by measurements utilizing pulsed high magnetic fields up to 40 T [67].

characteristic of the first-order transition coupled with the change of crystal lattice. The change in lattice parameters originates from the field destruction of orbital ordering. As seen in Fig. 11, the hysteresis region (hatched area) expands with decreasing temperature especially below about 20 K. In the case of the first-order phase transition, the transition from the metastable to the stable state occurs by overcoming a free-energy barrier. Since the thermal energy reduces with decrease in temperature, a larger (smaller) field than the thermodynamic value is needed to induce the transition from (to) the AF charge/orbital-ordered to (from) the FM metallic state. Thus the hysteresis between the field increasing and decreasing runs increases with the decrease of temperature.

4.2. Effect of discommensuration of doping level

The charge/orbital-ordering phenomena tend to be most stabilized when the band filling coincides with a rational number for the periodicity of the crystal lattice. In fact, the charge/orbital-ordered state in $Nd_{1-x}Sr_xMnO_3$ emerges only in the immediate vicinity of $x = 0.5$, as shown in Fig. 6. In perovskite manganites of which W is further reduced, such as $Pr_{1-x}Ca_xMnO_3$, however, the charge/orbital ordering of the similar CE type appears in a much broader range of x [50]. We have already shown in Fig. 6 the electronic phase diagram of $Pr_{1-x}Ca_xMnO_3$ $(0 < x < 0.5)$ [58]. In Fig. 6, the ferromagnetic and metallic state is not realized at zero magnetic field and at ambient pressure due to the reduced W, while the ferromagnetic but insulating phase appears for $0.15 < x < 0.3$. With further increase in x, the charge/orbital-ordered state with 1 : 1 ordering of Mn^{3+}/Mn^{4+} appears for $x > 0.3$. As an earlier neutron diffraction study [50] reported, the charge/orbital ordering exists in a broad range of x $(0.3 < x < 0.75)$, where the pattern of spin, charge and orbital ordering is basically described by that of $x = 0.5$. The coupling of spins along the c-axis is antiferromagnetic at $x = 0.5$, while the spin arrangement is not antiferromagnetic (or collinear) but canted for $x < 0.5$. As the doping level deviates from the commensurate value of 0.5, extra electrons are doped on the Mn^{4+} sites in a naive sense. To explain the modification of the arrangement of spins along the c-axis, Jirak et al. [50] postulated that the extra electrons hop along the c-axis mediating the ferromagnetic double exchange interaction. (This is analogous to the lightly hole-doped case of $LaMnO_3$, where the canted antiferromagnetic spin structure is realized due to the hole motion along the c-axis [6].) Such an effect of extra electrons on the magnetic structure should be enhanced with decrease in x from 0.5. In fact, neutron diffraction studies [50,51] have revealed that the coupling of spins along the c-axis becomes almost ferromagnetic at $x = 0.3$ in spite of that the CE-type ordering is maintained within the orthorhombic ab-plane.

Fig. 12 (left) exemplifies the magnetic field dependence of the resistvity (at 4.2 K) and the magnetization (at 5 K) for a $Pr_{1-x}Ca_xMnO_3$ $(x = 0.3)$ crystal [57]. Although the crystal of $x = 0.3$ undergoes the charge/orbital ordering transition at $T_{CO} \approx 200$ K [51], it changes to the metallic state in a magnetic field. In the magnetization curve of Fig. 12, the transition from the canted AF to the fully spin-polarized (ferromagnetic) state is observed at about 3.5 T in the field increasing process. In accord with the behavior in magnetization, the resistivity shows an insulator to metal transition at ≈ 4 T. Because of the strong first-order nature, the transition is irreversible at low temperatures and the ferromagnetic and metallic state remains even after the magnetic field is removed [57]. The observed phenomenon was further investigated by neutron diffraction measurements [51,68]. Fig. 12 (right) shows the magnetic field dependence of the intensities of the ferromagnetic (top), antiferromagnetic (middle) and orbital superlattice (bottom) reflections which were all taken at 5 K. Corresponding to decrease in the antiferromagnetic and orbital-superlattice diffractions at 4 T, an increase is observed for the ferromagnetic one. Thus, the field-induced insulator–metal transition is confirmed to be accompanied by collapse of the charge/orbital-ordered state.

For the $Pr_{1-x}Ca_xMnO_3$ $(x = 0.3)$ crystal, a similar insulator to metal transition is induced by applying an external pressure [69–71] which increases one-electron bandwidth W (or transfer integral t).

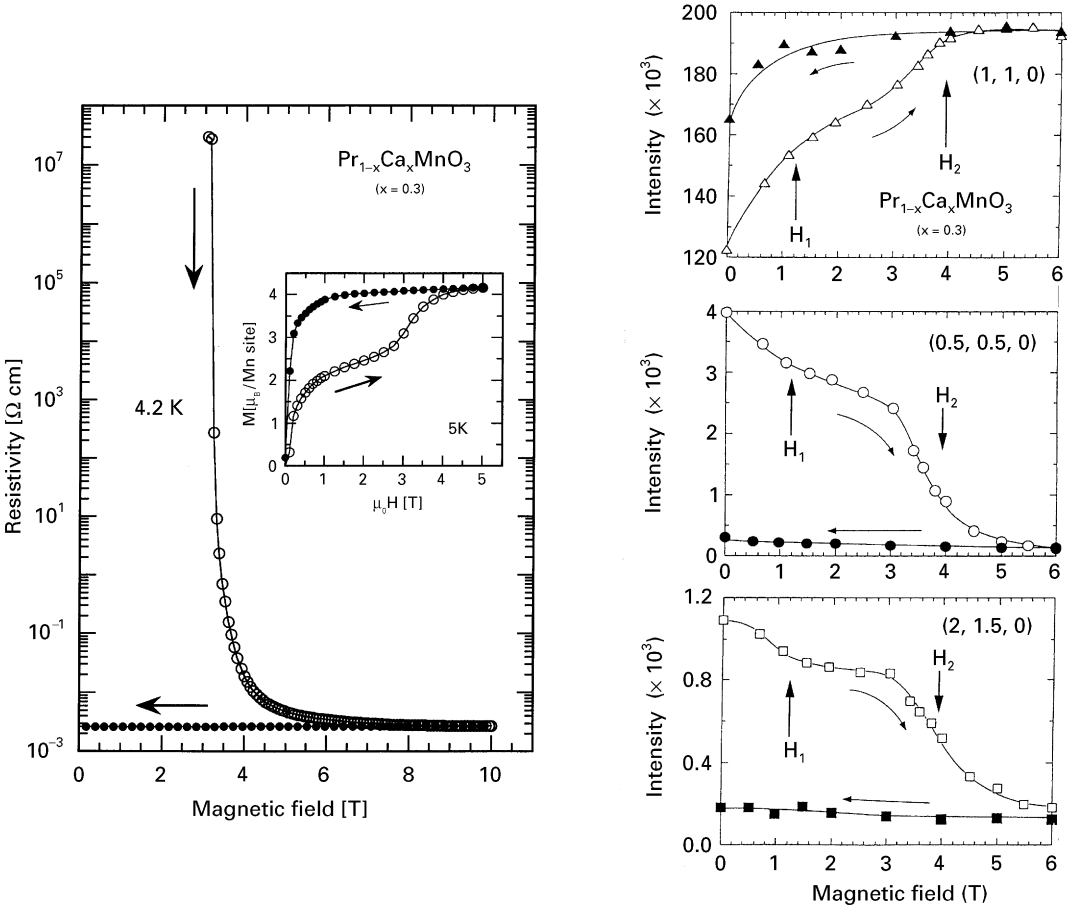

Fig. 12. Left: The resistivity at 4.2 K and magnetization at 5 K (inset) as a function of magnetic field for a $Pr_{1-x}Ca_xMnO_3$ ($x = 0.3$) crystal [57]. Right: The magnetic field dependence of the intensities of the ferromagnetic (top), antiferromagnetic (middle) and orbital superlattice (bottom) peaks obtained by neutron diffraction measurements at 5 K [48]. The superlattice reflection arises from the concomitant charge/orbital ordering. All the measurements were performed after the sample was cooled under zero field to a prescribed temperature.

In $Pr_{1-x}Ca_xMnO_3$, the dependence of the field-induced transition (or collapse of the charge/orbital-ordered state in a magnetic field) on the doping level has systematically been investigated for $0.3 < x < 0.5$ [58,67]. The x-dependent features are well demonstrated by the charge/orbital ordering phase diagram displayed on the magnetic field–temperature (H–T) plane as shown in Fig. 13. In this figure, the phase boundaries have been determined by the measurements of the magnetic field dependence of resistivity (ρ–H) and magnetization (M–H) at fixed temperatures. The charge/orbital ordering for $x = 0.5$ is so strong that the critical field to destruct the charge/orbital-ordered state becomes as large as about 27 T at 4.2 K, and a similar feature is also seen for $x = 0.45$ [67]. For $x < 0.4$, by contrast, the charge/orbital-ordered phase-region becomes remarkably shrunk, in particular at low temperatures. The averaged value (H_{av}) of the critical fields in the H-increasing and-decreasing runs at a constant temperature rather shows a decrease with decrease in temperature below ≈ 175 K ($dH_{av}/dT < 0$). In the case of $x = 0.3$, collapse of the charge/orbital-ordered state (i.e.,

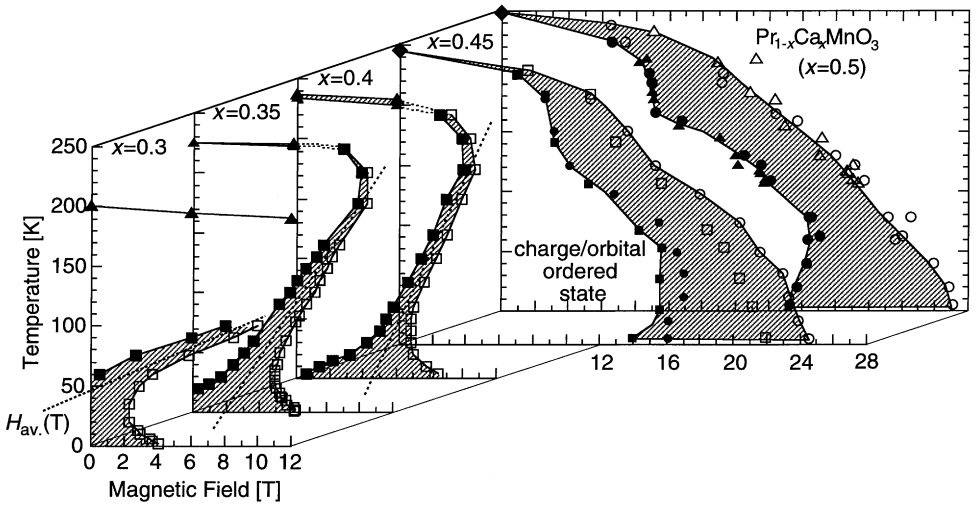

Fig. 13. The charge/orbital-ordered state of $Pr_{1-x}Ca_xMnO_3$ ($x = 0.5$, 0.45, 0.4, 0.35 and 0.3), which is plotted on the magnetic field-temperature plane [58,67]. The hatched area indicates the hysteresis region. In the cases of $x = 0.3$, 0.35 and 0.4, the lines of $H_{av}(T)$ at which the free energies of both the charge/orbital-ordered and the FM metallic states are supposed to be equal are indicated by dashed lines.

appearance of the FM metallic state) is realized by applying an external magnetic field of only several Tesla when the temperature is set below 50 K. Another noteworthy aspect in Fig. 13 is expansion of the field hysteresis with decreasing temperature, which is characteristic of the first order phase transition as mentioned above [61]. Such a variation of the charge/orbital-ordered phase with the doping level has been observed similarly for a further W-reduced system, $Nd_{1-x}Ca_xMnO_3$ [67,72]. The common feature for the modification of the phase diagram with x seems to be correlated with the action of the extra electron-type carriers in the CE-type structure [51]. Thermodynamically, excess entropy may be brought about in the charge/orbital-ordered state by the extra localized carriers and their related orbital degrees of freedom, which are pronounced as x deviates from 0.5. The excess entropy may reduce the stability of the charge-ordered state with decreasing temperature and cause the reduction in the critical magnetic field ($dH_{av}/dT < 0$) as observed in the case of $x < 0.4$ in Fig. 13. In reality, however, the microscopic phase separation into the $x \approx 0.5$ charge-ordered state and the $x < 0.5$ ferromagnetic state should be also taken into account for a deeper understanding of the present features for $x < 0.5$ systems.

5. CMR of the layered-structure manganites $La_{2-2x}Sr_{1+2x}Mn_2O_7$

The title compounds correspond to the $n = 2$ layered perovskite structures (see the inset to Fig. 14) with the MnO_2 bilayer in a repeated unit. Taking the Mn^{3+}-based compound, $La_2Sr_1Mn_2O_7$ ($x = 0$), as the parent insulator, the composition x stands for the nominal hole number per Mn site. Fig. 14 shows the temperature dependence of the ρ_{ab} in the series of Ruddlesden–Popper phases [$(La,Sr)_{n+1}Mn_nO_{3n+1}$; $n = 1,2$ and infinite] with the nominal hole concentration fixed at $x = 0.3$ [73]. In the pseudo-cubic ($n = \infty$) compound, the drop of the resistivity at ≈ 360 K corresponds to the onset of ferromagnetic ordering. The $n = 1$ phase with an isolated MnO_2 sheet, on the other hand, does not undergo the ferromagnetic transition and remains insulating down to the

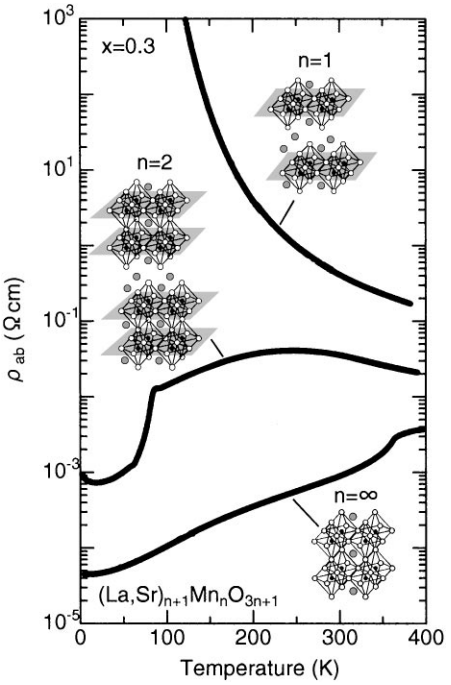

Fig. 14. The temperature dependence of in-plane resistivity (ρ_{ab}) for $n = 1$, 2, and ∞ members of the series of Ruddlesden-Popper phases, $(La,Sr)_{n+1}Mn_nO_{3n+1}$. The nominal hole concentration is fixed at $x = 0.3$. The inset shows the crystal structures of $(La,Sr)_{n+1}Mn_nO_{3n+1}$ ($n = 1$, 2, and ∞).

lowest temperature, perhaps due to the charge ordering instability [65,74]. In the $n = 2$ compound, ρ_{ab} shows a broad maximum around 270 K, and then metallic temperature dependence, followed by the sharp decrease at 90 K corresponding to the three-dimensional (3D) magnetic transition. (Concerning some controversy about the temperature dependence of the resistivity above the 3D transition temperature in this specific compound, see also Ref. [75].)

The temperature dependence of in-plane resistivity (ρ_{ab}) and c-axis resistivity (ρ_c) for this $x = 0.3$ single crystal shows a highly anisotropic behavior [76]. The ρ_c shows a sharp maximum at $T^c_{max} \approx 100$ K and semiconducting temperature dependence above T^c_{max} while a metallic-like behavior below T^c_{max}. Compared with the magnetization data, the steep drop of ρ_c below T^c_{max} has an intimate connection to the 3D ferromagnetic spin ordering. By contrast, ρ_{ab} shows a broad maximum at $T^{ab}_{max} \approx 270$ K where the slope of inverse magnetization deviates from the Curie–Weiss law. This implies that the in-plane two-dimensional (2D) ferromagnetic correlation evolves with decrease of temperature below T^{ab}_{max} that is far above T^c_{max}. The anisotropy of resistivity is as large as $\rho_c/\rho_{ab} \approx 10^3$ at room temperature, yet further increases with decrease of temperature and reaches such a large value as $\rho_c/\rho_{ab} \approx 10^4$ at T^c_{max}.

The isothermal MR curves with application of magnetic field along the c-axis are shown in Fig. 15 [76] for the in-plane and interplane components together with the magnetization curves at characteristic temperatures; around T^{ab}_{max} (273 K), T^c_{max} (100 K) and enough low temperature (4.2 K) with almost full spin polarization. Large MR is observed for the both components due to the enhanced in-plane and interplane ferromagnetic correlations at 273 K and more conspicuously at 100 K. In particular, the interplane MR at 100 K is extremely large ($\rho_c(H)/\rho_c(0) \approx 10^{-4}$ at 5 T) due to the field-induced incoherent–coherent transition for the c-axis charge transport at this temperature.

In the low-temperature case at 4.2 K, ρ_c drastically decreases in a low-field region in accord with the magnetization process, and becomes constant when the magnetization saturates above an external field of about 0.5 T. This MR behavior has been interpreted in terms of the interplane tunneling MR. According to the neutron scattering study [77], the ferromagnetic 3D ordering sets in below T^c_{max}, but the in-plane ferromagnetically ordered spins begins to cant between the inter-bilayer units, and below $T_N = 60$ K shows the layered-type antiferromagnetic ordering. In the antiferromagnetic state, the ferromagnetically ordered bilayers couple antiferromagnetically with the easy axis along the c-axis (perpendicular to the plane). The interplane antiferromagnetic interaction is extremely weak as compared with the in-plane ferromagnetic interaction, being inherent to the quasi-2D structure. Such an interplane antiferromagnetic coupling should block the interplane tunneling of the spin-polarized electrons, although the interlayer coupling mode should contain a high density of domain walls, i.e., the ferromagnetic interlayer coupling mode. (Such

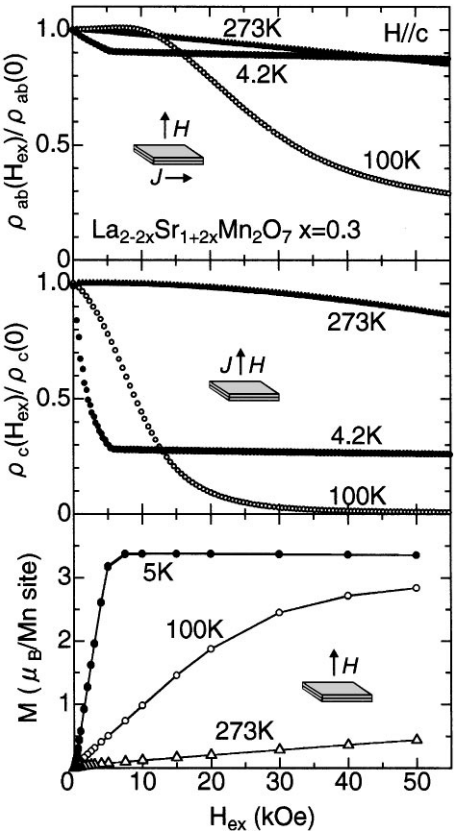

Fig. 15. Normalized in-plane (ρ_{ab}: top panel) and (B) interplane (ρ_c; middle panel) resistivity and (C) magnetization (M; bottom panel) as a function of H applied parallel to the c-axis at 4.2, 100, and 273 K for a $La_{2-x}Sr_{1+2x}Mn_2O_7$ ($x = 0.3$) crystal.

a ferromagnetically interlayer-coupled part as a defect may serve as a leaky current path along the c-axis.) By applying a magnetic field, however, a sort of metamagnetic transition takes place at a very low field, say 0.05 T, due to an extremely weak antiferromagnetic interlayer coupling, and accordingly the carrier-blocking boundaries should be removed. Such a field-switching of the spin structure in coincidence with the tunneling-type MR has in fact been confirmed by a neutron scattering study [77]. It is worth noting that the removal of the interlayer blocking domain-boundary also affects the in-plane charge dynamics as seen the low-field MR for the in-plane component at 4.2 K (top panel of Fig. 15). Thus, the $x = 0.3$ bilayered manganties can be viewed as an infinite stack of the spin valves.

The charge transport properties including the MR characteristics in these bilayer manganites are observed to be quite sensitive to the band filling or hole-doping level even more than in the aforementioned case of the pseudo-cubic perovskite manganites. This may be related to the variation of the orbital occupancy of the e_g conduction band due to the layered structure. The tetragonal crystal field in the layered structure generally tends to favor the $3z^2 - r^2$ orbital state. However, the in-plane 2D band dispersion should be larger for the $x^2 - y^2$ state than for $3z^2 - r^2$ state. Such a competition between the crystal field energy and the electron kinetic energy appears to cause the complex variation of the magnetic state and the lattice distortion as well as the magnetoelastic phenomena in this class of layered manganites [78]. For example, in the $x = 0.4$ crystal [79], both of the in-plane and interplane resistivity show a semiconducting increase with decrease of temperature down to T_C ($= 121$ K) with activation energy of 30–40 meV, though the anisotropic ratio of the resistivity is still as large as 10^2 , in contrast to the case of $x = 0.3$. At around T_C ($= 121$ K), both of the ρ_{ab} and ρ_c show a steep decrease by more than two orders of magnitude, showing a metallic behavior below T_C (although accompanied by localization behavior below about 20 K). By application of magnetic fields, the resistivity above T_C is appreciably suppressed, putting the resistivity maximum towards higher temperature. Recent extensive studies [80–82] have been revealing the strong charge/orbital correlation and associated dynamical lattice distortion (cooperative Jahn–Teller type) immediately above T_C where the CMR effect is most pronounced. Reflecting the simple 3D ferromagnetic spin structure in the ground state, however, such an interplane tunneling MR as observed for the $x = 0.3$ crystal does not show up in this $x = 0.4$ crystal.

With further increase of x, the ground state tends to show the spin canting within the bilayer unit, and its canting angle increases as x is increased from $x = 0.4$ to 0.5 [83], perhaps reflecting the increasing component of the $x^2 - y^2$ orbital state. For $x \approx 0.5$, the ground state of

$La_{2-x}Sr_{1+x}Mn_2O_7$ appears to be in the layered antiferromagnetic state, where the ferromagnetic single layer couples antiferromagnetically with each other within the bilayer unit [83,84]. The charge ordering transition associated by the orbital ordering as observed for the $x = 0.5$ single-layered and narrow-bandwidth perovskite manganites appears also at $x = 0.5$ in this $n = 2$ member manganite around 220 K [85]. However, as the temperature is decreased below 120 K, the charge ordering is again melted and the ground state is turned into the aforementioned layered antiferromagnetic state [86], perhaps reflecting the change in the orbital ordering pattern. Many unconventional features arising from the 2D nature of the carrier motion and the strong charge/orbital fluctuation are now being unraveled in the layered manganites, whose favorable simple structure and low-dimensionality may be a touchstone for the model for the spin-charge-orbital correlations in the magnetic oxides.

6. Concluding remarks

Fundamental features of the colossal magnetoresistive (CMR) manganites with perovskite-related structures have been described. The main advantage of the perovskites is the capability of controlling the band filling and the bandwidth, which are both important physical parameters for the strongly correlated electron system or strongly coupled electron-lattice system like the CMR manganites. First, we have seen a prototypical example of the double-exchange (DE) manganite, that is the case of $La_{1-x}Sr_xMnO_3$, whose MR near T_C can well be described by the canonical DE model. Even in that case, however, in particular near the metal-insulator compositional (x) phase boundary, we see ample examples of deviation from the simplest DE model. Those are ascribed partly to the Jahn–Teller-type electron-lattice coupling, which causes dynamical Jahn–Teller distortion or small polaron conduction above T_C. In other words, the hole-doping level (concentration of nominal mobile Mn^{4+} species in the Jahn–Teller Mn^{3+}-ion background) is not enough to extinguish the orbital "moment". This might be true also in the ferromagnetic metallic state. In fact, some anomalous features show up even in the metallic ground state, such as very high residual resistivity and minimal Drude (or quasi-particle spectral) weight in spite of seemingly insignificant mass-renormalization effect. In the ferromagnetic metallic ground state, the conduction electron spin is fully polarized (i.e., no spin degree of freedom left) and hence the anomalous features may originate from the carrier scattering process by orbital correlation or orbital fluctuation. However, most of the problems are left to be solved in the future.

In manganite systems with a narrower bandwidth than $La_{1-x}Sr_xMnO_3$, even more complex but intriguing features emerge due to the competition between the DE and other generic instabilities, such as antiferromagnetic superexchange, orbital-ordering, charge-ordering, and orbital-lattice (Jahn–Teller type) interactions. A complex electronic phase diagrams are presented for several $RE_{1-x}AE_xMnO_3$ (RE = La, Pr, Nd, and Sm; AE = Sr and Ca) as a function of the doping level, where the charge/orbital/spin ordering occasionally shows up near the doping level of $x = 1/2$. Conspicuous phase transition from a charge/orbital ordered state to a ferromagnetic metal is caused by application of an external magnetic field. More lately, it has been demonstrated that other external stimuli than magnetic field, such as impurity (e.g. Cr^{3+})-doping on the Mn site [87], current-injection [88], and photo-irradiation [89] or X-ray irradiation [90] can drive such a phase transformation, although the transitions remain within the spatially local area. These phenomena have been attracting great interest in the context of unconventional phase control of the magnetic and electronic states in the magnetic oxides.

In addition to the conventional pseudocubic manganites, the layered structure manganites or so-called Ruddlesden–Popper series are also the important systems endowed with CMR. Due to the confinement of the DE carriers within the plane, the magnetic interaction in the layered manganite is extremely anisotropic, and other competitive interactions such as charge and orbital ordering correlations become relatively important. We have seen versatile phenomena arising from such a two-dimensionality, while many unconventional features are now being unraveled. One such example is

the interplane tunneling MR which arises from the weak antiferromagnetic inter-bilayer coupling between the ferromagnetic–metallic Mn–O bilayer-sheets in $La_{2-2x}Sr_{1+2x}Mn_2O_7$ ($x = 0.3$) and is reviewed also in the article by Gupta and Sun of this volume with a broader perspective.

Acknowledgements

The authors would like to thank T. Kimura, A. Asamitsu, T. Okuda, and E. Saitoh for their help in preparation of the manuscript. The work was in part supported by NEDO and by a Grant-In-Aid for the COE Project from the Ministry of Education, Japan.

References

[1] For a more comprehensive review, see for example, Y. Tokura (Ed.), Colossal Magnetoresistive Oxides, Gordon & Breach Science Publishers, London, 1999.
[2] C.W. Searle, S.T. Wang, Can. J. Phys. 47 (1969) 2023.
[3] K. Kubo, N. Ohata, J. Phys. Soc. Jpn. 33 (1972) 21.
[4] C. Zener, Phys. Rev. 82 (1951) 403.
[5] P.W. Anderson, H. Hasegawa, Phys. Rev. 100 (1955) 67.
[6] P.-G. de Gennes, Phys. Rev. 118 (1960) 141.
[7] R.M. Kusters, D.A. Singleton, D.A. Keen, R. McGreevy, W. Hayes, Physica B 155 (1989) 362.
[8] K. Chabara, T. Ohno, M. Kasai, Y. Kozono, Appl. Phys. Lett. 63 (1993) 1990.
[9] R. von Helmolt, J. Wocker, B. Holzapfel, M. Schultz, K. Samwer, Phys. Rev. Lett. 71 (1993) 2331.
[10] S. Jin, T.H. Tiefel, M. mcCormack, R.A. Fastnacht, R. Ramesh, L.H. Chen, Science 264 (1994) 413.
[11] Y. Tokura, A. Urushibara, Y. Moritomo, T. Arima, A. Asamitsu, G. Kido, N. Furukawa, J. Phys. Soc. Jpn. 63 (1994) 3931.
[12] A. Asamitsu, Y. Moritomo, Y. Tomioka, T. Arima, Y. Tokura, Nature 373 (1995) 407.
[13] M. Imada, A. Fujimori, Y. Tokura, Rev. Mod. Phys. 70 (1998) 1039.
[14] J. Kanamori, J. Appl. Phys. 31 (1960) 14S.
[15] For a review, see, J.B. Goodenogh, J.M. Longon, in: K.-H. Hellwege, O. Madelung (Eds.), Magnetic and Other Properties of Oxides and Related Compounds, Landolt-Bornstein, New Series, Group III, vol.4, Pt. a Springer, Berlin, 1970.
[16] E.O. Wollan, W.C. Koehler, Phys. Rev. 100 (1955) 54.
[17] A. Urushibara, Y. Moritomo, T. Arima, A. Asamitsu, G. Kido, Y. Tokura, Phys. Rev. B 51 (1995) 14103.
[18] H. Kawano, R. Kajimoto, M. Kubota, H. Yoshizawa, Phys. Rev. B 53 R14709, (1996) 2202.
[19] N. Furukawa, J. Phys. Soc. Jpn. 63 (1994) 3214.
[20] M.F. Hundley, M. Hawley, R.H. Heffner, Q.X. Jia, J.J. Neumeier, J. Tesmer, J.D. Thompson, X.D. Wu, Appl. Phys. Lett. 67 (1995) 860.
[21] A.J. Millis, P.B. Littlewood, B.I. Shraiman, Phys. Rev. Lett. 74 (1995) 5144.
[22] A.J. Millis, R. Mueller, B.I. Shraiman, Phys. Rev. B 54 (1996) 5405.
[23] H. Roder, J. Zang, A.R. Bishop, Phys. Rev. Lett. 76 (1996) 1356.
[24] P. Dai, Jiandi Zhang, H.A. Mook, S.-H. Liou, P.A. Dowben, E.W. Plummer, Phys. Rev. B 54 (1996) R3694.
[25] P.G. Radaelli, D.E. Cox, M. Marezio, S.-W. Cheong, P.E. Schiffer, A.P. Ramirez, Phys. Rev. Lett. 75 (1995) 4488.
[26] C.M. Varma, Phys. Rev. B 54 (1996) 7328.
[27] M. Kataoka, Chechoslovak J. Phys. 46 (1996) 1857.
[28] M. Kataoka, M. Tachiki, Physica B 237–238 (1997) 24.
[29] K.I. Kugel, D.I. Khomskii, Sov. Phys. JETP 37 (1973) 725.
[30] S. Inagaki, J. Phys. Soc. Jpn. 39 (1975) 596.
[31] Despina Louca et al., Phys. Rev. B 56 (1997) R8475.
[32] S. Yoon, H. Liu, G. Schollerer, S.L. Cooper, P.D. Han, D.A. Payne, S.-W. Cheong, Z. Fisk, Phys. Rev. B 58 (1988) 2795.
[33] T. Okuda, A. Asamitsu, Y. Tomioka, T. Kimura, Y. Taguchi, Y. Tokura, Phys. Rev. Lett. 81 (1998) 3203.
[34] Y. Yamada, O. Hino, S. Nohdo, R. Kanao, T. Inami, S. Katano, Phys. Rev. Lett. 77 (1996) 904.
[35] J.-S. Zhou, J.B. Goodenogh, A. Asamitsu, Y. Tokura, Phys. Rev. Lett. 79 (1997) 3234.
[36] B.F. Woodfield, M.L. Wilson, J.M. Byers, Phys. Rev. Lett. 78 (1997) 3201.
[37] A. Asamitsu, Y. Tokura, Phys. Rev. B 58 (1998) 47.
[38] D.B. McWhan, J.P. Remeika, Phys. Rev. B 2 (1970) 3734.
[39] D.B. McWhan, A. Menth, J.P. Remeika, W.F. Brinkman, T.M. Rice, Phys. Rev. B 7 (1973) 1920.
[40] Y. Tokura, Y. Taguchi, Y. Okada, Y. Fujishima, T. Arima, K. Kumagai, Y. Iye, Phys. Rev. Lett. 70 (1993) 2126.
[41] K. Kumagai, T. Suzuki, Y. Taguchi, Y. Okada, Y. Fujishima, Y. Tokura, Phys. Rev. B 48 (1993) 7636.
[42] Y. Moritomo, A. Asamitsu, Y. Tokura, Phys. Rev. B 56 (1997) 12190.
[43] N. Furukawa, J. Phys. Soc. Jpn. 64 (1995) 3164.
[44] Y. Okimoto, T. Katsufuji, T. Ishikawa, A. Urushibara, T. Arima, Y. Tokura, Phys. Rev. Lett. 75 (1995) 109.
[45] S. Ishihara, M. Yamanaka, N. Nagaosa, Phys. Rev. B 56 (1997) 686.
[46] M. Imada, J. Phys. Soc. Jpn. 67 (1998) 45.
[47] A. Moreo, S. Yunoki, E. Dagotto, Science 283 (1999) 2034, and references cited therein.
[48] Y. Tokura, Y. Tomioka, H. Kuwahara, A. Asamitsu, Y. Moritomo, M. Kasai, J. Appl. Phys. 79 (1996) 5288.
[49] J.B. Goodenough, Phys. Rev. 100 (1955) 564.
[50] Z. Jirak, S. Krupicka, Z. Simsa, M. Dlouha, Z. Vlatislav, J. Magn. Magn. Mater. 53 (1985) 153.
[51] H. Yoshizawa, H. Kawano, Y. Tomioka, Y. Tokura, Phys. Rev. B 52 (1995) R1345.

[52] H. Kuwahara, Y. Tomioka, A. Asamitsu, Y. Moritomo, Y. Tokura, Science 270 (1995) 961.
[53] H. Kawano, R. Kajimoto, H. Yoshizawa, Y. Tomioka, H. Kuwahara, Y. Tokura, Phys. Rev. Lett. 78 (1997) 4253.
[54] H. Kuwahara, T. Okuda, Y. Tomioka, A. Asamitsu, Y. Tokura, Phys. Rev. Lett. 82 (1999) 4316.
[55] Y. Moritomo, T. Akimoto, A. Nakamura, K. Hirota, K. Ohoyama, M. Ohashi, Phys. Rev. B 58 (1998) 5544.
[56] R. Maezono, S. Ishihara, N. Nagaosa, Phys. Rev. B 58 (1998) 11583.
[57] Y. Tomioka, A. Asamitsu, Y. Moritomo, Y. Tokura, J. Phys. Soc. Jpn. 64 (1995) 3626.
[58] Y. Tomioka, A. Asamitsu, H. Kuwahara, Y. Tokura, Phys. Rev. B 53 (1996) R1689.
[59] H.Y. Hwang, S.-W. Cheong, P.G. Radaelli, M. Marezio, B. Batlogg, Phys. Rev. Lett. 75 (1995) 914.
[60] Y. Tomioka, H. Kuwahara, A. Asamitsu, M. Kasai, Y. Tokura, Appl. Phys. Lett. 70 (1997) 3609.
[61] H. Kuwahara, Y. Tomioka, A. Asamitsu, Y. Moritomo, Y. Tokura, Science 270 (1995) 961.
[62] Y. Tomioka, A. Asamitsu, H. Kuwahara, Y. Moritomo, M. Kasai, R. Kumai, Y. Tokura, Physica B 237-238 (1997) 6.
[63] P.G. Radaelli, D.E. Cox, M. Marezio, S.-W. Cheong, P.E. Shiffer, A.P. Ramirez, Phys. Rev. Lett. 75 (1995) 4488.
[64] P.G. Radaelli, D.E. Cox, M. Marezio, S.-W. Cheong, Phys. Rev. B 55 (1997) 3015.
[65] B.J. Sternlieb, J.P. Hill, U.C. Wildgruber, G.M. Luke, B. Nachumi, Y. Moritomo, Y. Tokura, Phys. Rev. Lett. 76 (1996) 2169.
[66] Y. Tomioka, A. Asamitsu, Y. Moritomo, H. Kuwahara, Y. Tokura, Phys. Rev. Lett. 74 (1995) 5108.
[67] M. Tokunaga, N. Miura, Y. Tomioka, Y. Tokura, Phys. Rev. B 57 (1998) 5259.
[68] H. Yoshizawa, H. Kawano, Y. Tomioka, Y. Tokura, J. Phys. Soc. Jpn. 65 (1996) 1043.
[69] H.Y. Hwang, T.T.M. Palstra, S.-W. Cheong, B. Batlogg, Phys. Rev. B 52 (1995) 15046.
[70] Y. Moritomo, H. Kuwahara, Y. Tomioka, Y. Tokura, Phys. Rev. B 55 (1997) 7549.
[71] H. Yoshizawa, R. Kajimoto, H. Kawano, Y. Tomioka, Y. Tokura, Rev. B 55 (1997) 2729.
[72] K. Liu, X.W. Wu, K.H. Ahn, T. Sulchek, C.L. Chien, J.Q. Xiao, Phys. Rev. B 54 (1996) 3007.
[73] T. Kimura, Y. Tomioka, T. Okuda, H. Kuwahara, A. Asamitsu, Y. Tokura, in: M.F. Hundley, J.H. Nickel, R. Ramesh, Y. Tokura, (Eds.), MRS Symposium Proceedings, vol. 494, Science and Technology of Magnetic Oxides, pp. 347, Materials Research Society, Warrendale, 1998.
[74] Y. Moritomo, Y. Tomioka, A. Asamitsu, Y. Tokura, Y. Matsui, Phys. Rev. B 51 (1995) 3297.
[75] Qing' An Li, K.E. Gray, J.F. Mitchell, Phys. Rev. B 59 (1999) 9357.
[76] T. Kimura, Y. Tomioka, H. Kuwahara, A. Asamitsu, M. Tamura, Y. Tokura, Science 274 (1996) 1698.
[77] T.G. Perring, G. Aeppli, T. Kimura, Y. Tokura, M.A. Adams, Phys. Rev. B 58 (1998) R14698.
[78] T. Kimura, Y. Tomioka, A. Asamitsu, Y. Tokura, Phys. Rev. Lett. 81 (1998) 5920.
[79] Y. Moritomo, A. Asamitsu, H. Kuwahara, Y. Tokura, Nature 380 (1996) 141.
[80] J.F. Mitchell, D.N. Argyriou, J.D. Jorgensen, D.G. Hinks, C.D. Potter, S.D. Bader, Phys. Rev. B 55 (1997) 63.
[81] D.N. Argyriou, J.F. Mitchell, C.D. Potter, S.D. Bader, R. Kleb, J.D. Jorgensen, Phys. Rev. B 55 (1997) R11965.
[82] T. Ishikawa, T. Kimura, T. Katsufuji, Y. Tokura, Phys. Rev. B 57 (1998) R8079.
[83] K. Hirota, Y. Moritomo, H. Fujioka, M. Kubota, H. Yoshizawa, Y. Endoh, J. Phys. Soc. Jpn. 67 (1998) 3380.
[84] P.D. Battle, D.E. Cox, M.A. Green, J.E. Millburn, L.E. Spring, P.G. Radaelli, P.M.J. Rosseinsky, J.F. Vente, Chem. Mater. 9 (1997) 1042.
[85] J.Q. Li, Y. Matsui, T. Kimura, Y. Tokura, Phys. Rev. B 57 (1998) R3205.
[86] T. Kimura, R. Kumai, Y. Tokura, J.Q. Li, Y. Matsui, Phys. Rev. B 58 (1998) 11081.
[87] B. Raveau, A. Maignan, C. Martin, J. Solid State Chem. 130 (1997) 162.
[88] A. Asamitsu, Y. Tomioka, H. Kuwahara, Y. Tokura, Nature 388 (1997) 50.
[89] K. Miyano, T. Tanaka, Y. Tomioka, Y. Tokura, Phys. Rev. Lett. 78 (1997) 4257.
[90] V. Kiryukhin, D. Casa, J.P. Hill, B. Keimer, A. Vigliante, Y. Tomioka, Y. Tokura, Nature 386 (1997) 813.